Link between melt-impregnation and metamorphism of Atlantis Massif peridotite (IODP Expedition 357)

Contributions to Mineralogy and Petrology (2022) 177:106
https://doi.org/10.1007/s00410-022-01968-9

ORIGINAL PAPER

Link between melt-impregnation and metamorphism of Atlantis Massif peridotite (IODP Expedition 357)

Scott A. Whattam[1] · Jan C. M. De Hoog[2] · Matthew I. Leybourne[3] · Mohamed Zaki Khedr[4]

Received: 9 April 2022 / Accepted: 5 October 2022

Abstract

IODP Expedition 357 drilled 17 shallow sites scattered over ~ 10 km in the west to east spreading direction across the Atlantis Massif oceanic core complex (OCC, MAR, 30 ºN). Mantle exposed in the footwall of the Atlantic Massif OCC is nearly wholly serpentinized (80–100%) harzburgite and subordinate dunite. A recent whole-rock chemistry study by Whattam et al. (Chemical Geology 594. 10.1016/j.chemgeo.2021.120681, 2022) subdivides Atlantis Massif peridotites into: Type I fluid–rock dominated serpentinite, which exhibits almost nil evidence of melt-impregnation or silica metasomatism; Type II melt–rock dominated, mafic melt-impregnated serpentinite; and Type III melt–rock dominated Si-metasomatized serpentinite. In this study, on the basis of EPMA, three kinds of Cr–spinel are distinguished in Expedition 357 serpentinite: (I) primary, unmetamorphosed mantle array, (II) low-Ti metamorphosed, and (III) high-Ti melt reacted. All Cr–spinel of western site Type I serpentinite is unmetamorphosed ($n = 34$) and comprises 68% of all unmetamorphosed Cr–spinel. Metamorphosed Cr–spinel ($n = 100$) are the most abundant and occur in the central and eastern site Type II and Type III serpentinite, whereas melt-reacted Cr–spinel and chromite are restricted to the central sites and occur predominantly in serpentinized dunite. Estimates of the degree of melt extraction of Type I serpentinite using $F = 10\ln(\text{spinel Cr\#}) + 24$ are ~ 9–17%. Fugacity calculations of primary, unmetamorphosed Cr–spinel yield $\Delta\log(fO_2)_{FMQ}$ of − 1.7 to + 1.0 and calculations using olivine–spinel Mg–Fe exchange thermometry yield a mean closure temperature of 808 ± 39 °C. Mafic melt-impregnation resulted in Cr–spinel with anomalously high TiO_2 of 0.27–0.68 wt.% and production of Ti-rich chromite (up to 1.23 wt.% TiO_2). Greenschist facies metamorphism (< 500 °C) resulted in Mg–Fe^{2+} exchange between Cr–spinel and forsterite and anomalously low Cr–spinel Mg#; higher degrees of amphibolite facies metamorphism (~ 500–700 °C) also resulted in anomalously high Cr# due to Al–Cr exchange. As has been previously established, significant Al loss from chromite cores above 550 °C is the result of equilibration with fluids in equilibrium with chlorite, which may be valid for our samples. On the basis of Cr–spinel vs. whole-rock compositions, a clear relationship exists between melt-impregnation and metamorphism of central and eastern serpentinite, which we postulate to be the result of heat associated with magma injection and subsequent localized contact metamorphism. To our knowledge, such a relation between mafic melt-impregnation of peridotite and metamorphism (of peridotite) has not previously been established in general and specifically for the Atlantis Massif peridotite. Closure temperatures of 440–731 °C of metamorphosed Cr–spinel approximate greenschist to amphibolite facies metamorphic conditions.

Keywords IODP Expedition 357 · Atlantis Massif · Mantle peridotite · Melt-impregnation · Melt–rock reaction · Metamorphism · Greenschist facies · Amphibolite facies

Introduction

Oceanic core complexes (OCCs), such as the Atlantis Massif (30°N, Fig. 1a) of the Mid-Atlantic Ridge (MAR) represent segments of a slow spreading ridge comprising elevated seafloor massifs that display flat or gently curved upper surfaces with prominent corrugations or megamullions (Escartin et al. 2017; Tucholke et al. 1998). OCCs represent the most accessible parts for sampling of the lower oceanic crust

Communicated by Timothy L. Grove.

✉ Scott A. Whattam
sawhatta@gmail.com

Extended author information available on the last page of the article

Published online: 07 November 2022

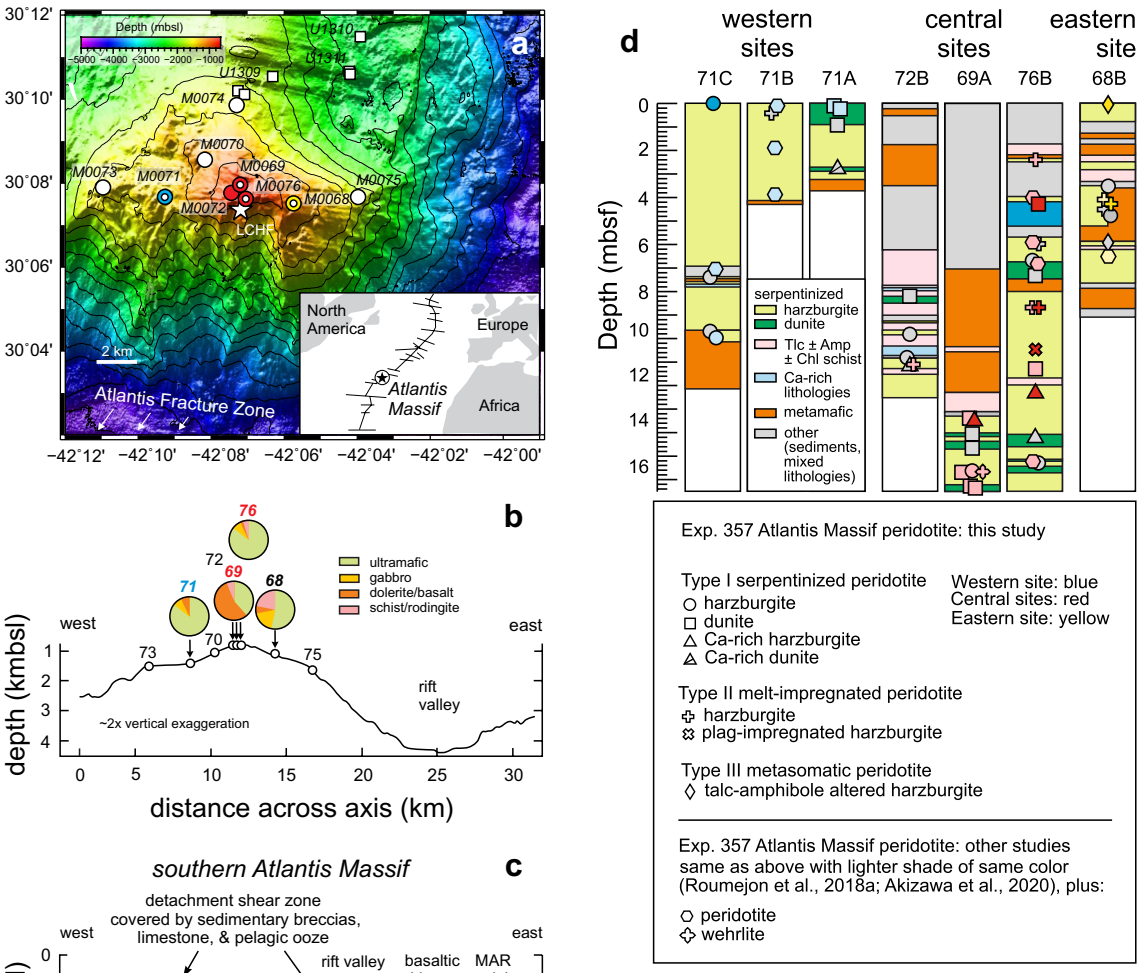

and upper mantle on the seafloor (Cann et al. 1997; Blackman et al. 1998; Tucholke et al. 1998). OCCs form uplifted footwall along detachment faults, i.e., large-offset low-angle normal faults. The upper mantle in OCCs is typically composed of dominantly harzburgite and dunite; these rocks are typically heavily serpentinized through interaction with seawater at a range of temperatures (Andreani et al. 2007; Boschi et al. 2006a, 2006b; Cannat, 1993; Früh-Green et al. 2004; Karson et al. 2006; Kelemen et al. 2007; Rouméjon et al. 2015, 2018a; Cann et al. 1997; Blackman et al. 1998).

Studies of abyssal and ophiolitic peridotite have shown that the compositional variability of lithospheric mantle at extensional settings such as the MAR is largely caused by reactive percolation of rising melts in the thermal boundary layer and subsequent melt–rock interaction as recorded by lithospheric peridotite. Melt–rock interactions inferred to have occurred in the lithospheric mantle at mid-ocean ridges have been documented from the study of troctolite–olivine gabbro suites sampled in ophiolites (Kelemen et al. 1995a, b, 1997; Borghini et al. 2007; Borghini and Rampone 2007; Renna and Tribuzio 2011; Sanfilippo and Tribuzio 2013; Sanfilippo et al. 2014) and at present-day oceanic ridges (Arai and Matsukage 1996; Dick and Natland 1996; Cannat et al. 1990; Suhr et al. 2008; Drouin et al. 2009; Sanfilippo et al. 2013). Considerable knowledge has also resulted from studies of Alpine–Apennine ophiolites, which are comprised predominantly of mantle peridotite, and are broadly thought to represent analogs of oceanic lithosphere formed at ocean/continent transition and slow- to ultraslow-spreading settings (e.g., Rampone and Piccardo 2000; Manatschal and Müntener 2009; Picazo et al. 2016). Melt–rock reactions have also been

◂**Fig. 1** **a** Bathymetric map centered on the southern wall of the Atlantis Massif (modified after Rouméjon et al. 2018a) showing the location of the Atlantis Massif on the western flank of the Mid-Atlantic Ridge axial valley and bordered to the south by the Atlantis Fracture Zone. Inset shows location of the Atlantis Massif at 30°N within the context of the greater MAR spreading system (modified from Kelley et al. 2001). Circles with numbers in italics and beginning with M00 represent drill hole locations of IODP Expedition 357 (Früh-Green et al. 2017, 2018). White circles are drill holes which did not yield peridotite; blue, red, and yellow circles represent western (M0071), central (M0069, M0072, M0076) and eastern (M0068) sites, respectively, which do yield peridotite and colored circles with a smaller white circle inside are sites in which peridotites were sampled in this study. The mineral phases used in this paper are from peridotite of this study and the studies of Rouméjon et al. (2018a) and Akizawa et al. (2020). The white squares represent sites (U1309, U1310, U1311) drilled during IODP Expediton 304/305 (Blackman et al. 2006) and the white star shows the location of the Lost City Hydrothermal Field (LCHF) (Kelley et al. 2001). **b** Bathymetry profile of the Atlantis Massif southern wall and the lithologic variations in Expedition 357 holes investigated in this study (M0071, M0069, M0076, M0068). Pie charts show percentages of dominant lithologies recovered based on core length. Modified from Früh-Green et al. (2017). **c** Sketch of the southern wall of the Atlantis Massif, which is dominated by variably altered peridotite with gabbroic lenses, which contrasts major gabbroic intrusions in the central core. Modified from Früh-Green et al. (2017). **d** Simplified depiction of predominant lithologies present in the seven drill holes which yield serpentinized peridotite (modified from Rouméjon et al. 2018a; see Früh-Green et al. 2018 for complete expedition drill hole vertical sections). The light gray symbols represent peridotite analyzed for whole-rock chemistry from the study of Whattam et al. (2022). Dark blue, red, and yellow symbols represent samples of western, central, and eastern serpentinized harzburgite and dunite analyzed for microprobe spinel analysis in this study; the light yellow, light blue and pink symbols represent samples analyzed for microprobe spinel and olivine analysis from the studies of Rouméjon et al. (2018a) and Akizawa et al. (2020), which are used in conjunction with our analyses. The sections are arranged from right to left according to longitude (see Fig. 1b) and from hole top to bottom. The central holes embody in situ segments of the detachment footwall, whereas the western and eastern site holes that yield rubbly intervals and sedimentary structures are talus and interpreted as artifacts of mass wasting and local faulting

documented in forearc, magmatic, plagioclase-bearing peridotite (Whattam et al. 2011).

These mantle 're-fertilization' reactions (e.gLenoir et al. 2001; Van der Wal and Bodinier 1996) entail two key processes: (i) a secondary partial melting event that produces the metasomatic agent (melt/fluid); and (ii) melt/fluid–peridotite interaction/reaction, which causes modal and compositional modifications in the residual peridotite. The reactive behavior of percolating melts during ascent from the partial melting region in the asthenosphere to the lithospheric mantle is related to progressive oversaturation in olivine and undersaturation in pyroxene (e.g., Kelemen1990; Kelemen et al. 1990, 1995a,b, 1997; Grove et al. 1992). This results in olivine crystallization and pyroxene dissolution at deeper and hotter spinel facies mantle depths, and the formation of replacive harzburgite and dunite. At shallower and colder lithospheric depths (i.e., plagioclase lherzolite stability field at < 30 km with pressures of ~ 0.5–1 GPa) percolating melts will crystallize plagioclase, together with pyroxene and/or olivine, thus producing plagioclase-rich impregnated peridotite (e.g., Arai and Matsukage 1996).

The percolation of melts by porous flow into mantle peridotite is accompanied by melt–rock interactions, whose effects are mainly controlled by physical parameters (temperature, pressure), composition of the reacting melt, melt–rock ratio and grainscale processes (Liang 2003; Morgan and Liang 2003, 2005). Such melt–rock interaction processes create significant modifications and are believed to be responsible for chemical variability of MORBs observed at a local to regional scale (e.g., Le Roux et al. 2002; Collier and Kelemen 2010; Lambart et al. 2013).

Melt–rock reactions in oceanic peridotite are thus well documented, but metamorphism of oceanic peridotite, apart from low-temperature metamorphism in the formation of serpentinite, and the possible relationship between melt–rock reaction and metamorphism, is less studied. Metamorphic processes of oceanic peridotite range from high-temperature recrystallization in the stability field of plagioclase peridotite (see above) to complete serpentinization (e.g., Burkhard and O'Neil 1988). Metamorphism of oceanic peridotite as documented by Cr–spinel (Evans and Frost 1975; Kapsiotis et al. 2011) and a study of komatiitic chromite (Barnes 2000) show that chromite compositions are influenced by metamorphic processes, particularly above 500 °C. In particular, metamorphosed chromite is significantly more iron rich than igneous precursors as a result of Mg–Fe exchange, particularly between olivine and spinel; and significant Al loss from chromite cores above 550 °C is the result of equilibration with fluids in equilibrium with chlorite (Barnes 2000).

In the case of the Atlantic Massif OCC, multiple generations of amphibole have been observed in Atlantis Massif gabbro that have been interpreted to represent progressive alteration from amphibolite to greenschist facies conditions during exhumation, with a second phase recording temperatures of ~ 500 °C (Schroeder and John 2004; Boschi et al. 2006a). However, greenschist and higher facies metamorphism has not yet been documented in Atlantis Massif peridotite.

International Ocean Discovery Program (IODP) Expedition 357 drilled 17 shallow sites across ~ 10 km in the west to east-spreading direction across the Atlantis Massif OCC (Figs. 1a-c). Mantle exposed in the footwall of Atlantic Massif OCC is nearly wholly serpentinized (80–100%) harzburgite with subordinate dunite. On the basis of a recent study of whole-rock chemistry, Expedition 357 Atlantis Massif peridotite is subdivided into Type I serpentinite, Type II melt-impregnated serpentinite and Type III silica metasomatized serpentinite (Whattam et al. 2022). Western site M0071 comprises entirely of Type I serpentinite and,

in addition to central site M0069, have compositions akin to abyssal peridotite subjected to predominant fluid–rock interactions associated with serpentinization. The remaining central and eastern sites comprise high percentages of Types II and III serpentinite and have compositions that point to predominant melt–rock interactions. In this contribution, we use major element chemistry of Cr–spinel of Types I, II, and III serpentinite of the Atlantis Massif recovered during Expedition 357 to document compositional modifications of Cr–spinel and chromite due to melt–rock interaction and metamorphism and investigate possible relations between melt-impregnation and sub-greenschist to amphibolitefacies metamorphism.

Geological setting

The Mid-Atlantic ridge (MAR) (Fig. 1a) is a classic example of a slow spreading center. The MAR is characterized by wide (up to 30 km) and deep (1–2 km) axial valleys bounded by uplifted shoulders and transient magma reserves (e.g., McDonald 1982). The fast-spreading East Pacific Rise, in contrast, exhibits much narrower to absent axial troughs (a few hundred meters wide) and a more continuous magma supply (e.g., Macdonald 1982; Karson 2002; Stewart et al. 2005). 'Oceanic core complexes' (OCCs), such as the Atlantis Massif (30°N, Fig. 1b) of the MAR are analogous to 'metamorphic core complexes' found in areas of extension in continental regions (e.g., John 1987).

The Ocean Drilling Program (ODP), Integrated Ocean Drilling Program (IODP), and the International Ocean Discovery Program (IODP) have drilled four OCCs. These include the Atlantis Bank, SW Indian Ridge (ODP Hole 735B, Dick et al. 2000), MARK (Mid-Atlantic Ridge Kane fracture zone) at 23°32′ N (ODP Leg 153, Sites 921–924, Cannat et al. 1995), MAR at 15°44′ N (ODP Leg 209, Site 1275, Kelemen et al. 2004) and the Atlantis Massif, the most thoroughly studied, which also hosts the off-axis, peridotite-hosted Lost City hydrothermal field (Kelley et al. 2001). The Atlantis Massif was drilled during IODP Expeditions 304/305 (Blackman et al. 2006) at Site U1309 and Expedition 357 (Fig. 1b) (Früh-Green et al. 2017, 2018).

The dome-shaped Atlantis Massif (Figs. 1b, c) is located on the western edge of the MAR axial valley where it intersects the Atlantis Fracture Zone (Fig. 1a). The OCC extends for 15–20 km from north to south parallel to the ridge and is 8–12 km wide. Low-angle detachment faulting (Cann et al. 1997; Blackman et al. 2002; Schroeder and John, 2004; Karson et al. 2006; Ildefonse et al. 2007) resulted in its exhumation. On the basis of 18 SHRIMP U/Pb zircon ages of oxide gabbro and felsic dike melt intrusions recovered from Hole U1309D, the age of the lithosphere of the Atlantis Massif is 1.28 ± 0.05 to 1.08 ± 0.07 Ma (Grimes et al. 2008). Submersible dives and dredging reveals that the dominant lithology of the Atlantis Massif is serpentinized peridotite (Blackman et al. 2002; Boschi et al. 2006a; Karson et al. 2006), focused principally along the southern and most elevated portion of the detachment (Fig. 1a, b). However, samples recovered during IODP Expeditions 304/305 to the north of Expedition 357 (Fig. 1a) are mostly mafic. The maximum depth of drill hole achieved during Expedition 304/305 was ~ 1500 m, and recovered lithologies are nearly entirely olivine-rich gabbro and troctolite (Drouin et al. 2009; Ferrando et al. 2018; Godard et al. 2009; Suhr et al. 2008). These geological observations reveal lithological and chronological variations in the footwall characterized by a decrease in peridotite moving from the segment end toward the north to more voluminous later-formed magmas in the footwall (Ildefonse et al. 2007).

IODP Expedition 357 cored 17 shallow holes at nine sites along the detachment fault of the Atlantis Massif with core lengths of approximately 1.3–16.5 m (Fig. 1d) and high recovery rates of ~ 75% (Früh-Green et al., 2016). Whereas one western site (M0071) and the two eastern sites (M0075, M0068) recovered fault scarp deposits, the central sites yielded in situ sequences. Most sites are aligned along the southern edge of the detachment fault by the Atlantis Fracture Zone wall (Fig. 1a). The northernmost hole (M0074) is located ~ 6 km north of the detachment southern edge, and ~ 1 km to the southwest of U1309D. IODP Expedition 357 recovered primarily serpentinized harzburgite with subordinate dunite and rare wehrlite with lesser amounts of variably altered mafic inclusions of basalt, gabbro, and dolerite within peridotite (Früh-Green et al. 2018; Rouméjon et al. 2018a; Akizawa et al., 2020). The extent of serpentinization of peridotite in the Atlantis Massif is typically > 80%, locally extensively oxidized and in many cases, alteration is related to mafic melt-impregnation, and commonly associated silica metasomatism (Rouméjon et al. 2018a, b; Liebmann et al. 2018; Whattam et al. 2022). Emplacement of the majority of mafic intrusions of dolerite (diabase) and gabbro occurred prior to serpentinization (Früh-Green et al. 2018).

Samples, petrography, and Cr–spinel textures

Peridotite samples of this study are from holes immediately adjacent to the transform fault scarp and drilled at the southern edge of the detachment fault surface (Fig. 1a). The stratigraphic location of samples from this study is shown in Fig. 1d. All samples were studied by petrographic microscopy (Fig. 2). Sample numbers and rock type names are taken directly from Früh-Green et al. (2017, Supplementary material) and serpentinite 'type' is from Whattam et al. (2022). All peridotites were subjected to high

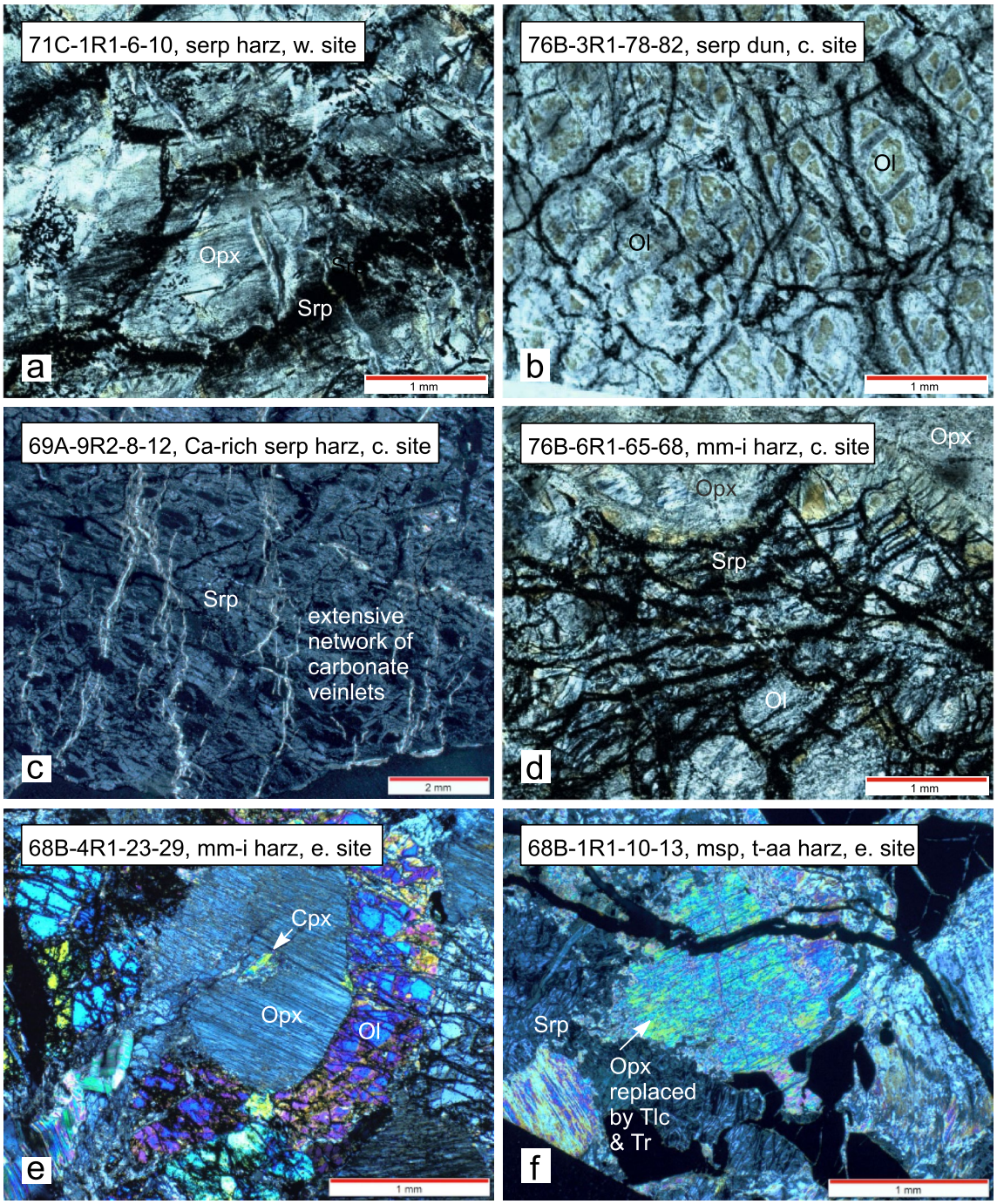

Fig. 2 Thin section images of Expedition 357. **a–c** Type I serpentinized peridotites, **d**, **e** Type II melt-impregnated peridotites, and **f** Type III metasomatic peridotite. 'Typical' completely serpentinized peridotite samples from **a** western site M0071C, **b** central site M0076B, and **c** central site M0069A, which show a Ca-rich harzburgite showing extensive network of carbonate veinlets. **d** Mafic melt-impregnated (mm-i) harzburgite from central site M0076B and **e** mm-i harzburgite from eastern site M0068B showing partially dissolved orthopyroxene porphyroclast mantled by secondary recrystallized olivine. **f** Talc-amphibole altered (t-aa) peridotite from eastern site M0068B, which is a harzburgite showing replacement of orthopyroxene by talc (Tlc) and tremolite (Tr). All images under cross-nicols. *mm-i* mafic melt-impregnated, *msp* metasomatic peridotite

degrees of serpentinization (> 80%). As the petrography of these serpentinites is provided in Whattam et al. (2022), we provide a simple summary of their petrography. Figure 2 provides micrographs of representative Types I, II, and III serpentinites.

Petrography

Type I serpentinite

Type I serpentinite (Fig. 2a-c) was formed after dominant harzburgite and lesser dunite protoliths. Serpentinization is most intense within olivine fractures and around grain peripheries (e.g., Fig. 2a, b). Classic mesh textures are common. Orthopyroxene is always altered to bastite in the harzburgite, but recognizable by remnant cleavage and parallel extinction. Olivine is 2–4 mm and orthopyroxene is typically smaller (< 2 mm). Brown to reddish-orange spinel is typically less than 0.5 mm but, in some cases, up to 4 mm, and occurs typically as isolated, anhedral grains. Serpentinized harzburgite comprises 80–90 vol. % olivine and 10–20 vol. % orthopyroxene; spinel ranges from 0 to 3 vol. % (Table 2). Relative to the harzburgite, orthopyroxene is absent and spinel is less common (0 to < 1 vol. %) in the dunite.

Some Type I serpentinite samples exhibit anomalously high CaO contents (up to 13 wt.%, Whattam et al. 2022), which we refer to as Type I Ca-rich serpentinite. These exhibit an extensive and densely concentrated network of ~ 0.1 mm-thick carbonate veinlets (Fig. 2c).

Type II melt-impregnated serpentinite

Melt-impregnated serpentinite (Fig. 2d, e) exhibit millimeter- to centimeter-scale mafic veins at the scale of the drill core, but are not obvious in thin section, perhaps due to small sample sizes. Bastite pseudomorphs after orthopyroxene are ~ 1–5 mm. Olivine and orthopyroxene modal percentages are 80–90 vol. % and 10–20 vol. %, respectively. Spinel ranges from absent to 2–3 vol. % of the mode. Other petrographic evidence to confirm melt-impregnation in some Type II serpentinite is the presence of plagioclase and replacive olivine (Whattam et al., 2022). Central sample (76B-7R1-81-83) has rare (< 0.5 vol. % of the mode), 0.5–0.7 mm plagioclase and another sample from eastern Site M0068B shows fresh 0.5–1 mm olivine constituting ~ 5 vol. % of the mode, partially mantling orthopyroxene (Fig. 2e).

Type III silica metasomatized serpentinite

Type III serpentinite was formed after harzburgite protoliths, and in this study, is from eastern site M0068B only (Fig. 1c), although Type III serpentinite also occurs in central sites (Früh-Green et al., 2018). This serpentinite is differentiated from all others on the basis of talc–amphibole alteration of orthopyroxene (Fig. 2f) and whole-rock chemistry, e.g., anomalously high SiO_2 of up to ~ 60 wt.% (Fruh-Green et al. 2018; Whattam et al. 2022). The modal percentages of olivine and orthopyroxene are ~ 70% and 30%, respectively. Spinel occupies about 2% of the mode. Orthopyroxene is 1–6 mm and brown spinel ranges from 0.5 to 2 mm. Spinel is always embedded in orthopyroxene.

Textural characteristics of spinel under SEM

On the basis of mineral chemistry, Cr–spinel and chromite of this study are subdivided into those that are (i) primary (unmetamorphosed); (ii) metamorphosed; and (iii) melt reacted (see Sects. 5 and 6). Reference to 'relative' degrees of metamorphism and melt–rock interaction indicates how far Cr–spinel in Cr–spinel Cr# vs. Mg# space, deviates from the unmetamorphosed, mantle array (see Sect. 6).

Spinel grain size is typically of the order of ~ 100 µm but ranges to 4 mm. Cr–spinel of the western Type I serpentinite is unmetamorphosed and SEM back-scatter electron (BSE) images show that Cr–spinel grains are large, smooth, light gray and unaltered (Fig. 3a), apart from localized minor alteration to magnetite along rims and fractures in some samples (Fig. 3b). Cr–spinel and chromite from the central and eastern sites show varying degrees of alteration depending on serpentinite type, the degree of metamorphism, and whether or not they have been subjected to melt–rock interaction. For example, weakly metamorphosed Cr–spinel of Type I serpentinite from some central sites show little alteration apart from the presence of thin rims or patches of Fe-rich zones (Fig. 3c), whereas both the core and bright, thick Fe-rich rims of moderately metamorphosed Cr–spinel show highly porous, pseudo-spongy texture (Fig. 3d, central Type II melt-impregnated harzburgite). Spinel from some Type II melt-impregnated serpentinite comprise both metamorphic and melt-reacted Cr–spinel (Fig. 3e, f). Whereas the least melt-reacted Cr–spinel is light gray with thin Fe-rich rims and zones (Fig. 3f), the highly melt-reacted chromite is even lighter gray and exhibit highly porous, spongy texture (Fig. 3 g, h).

Analytical methods

Electron probe micro-analyzer

Serpentinite samples spanning all three sites were chosen for electron probe micro-analyzer (EPMA) analysis. Quantitative major element mineral chemistry analyses were obtained on polished, carbon-coated thin sections using a JEOL JXA-8230 Electron Microprobe housed in the Queen's Facility for Isotope Research (QFIR), Department of Geological Sciences and Geological Engineering at Queen's University, Ontario, Canada. Operating conditions involved a 15 kV accelerating potential, beam current of 20 nA and a focused beam diameter of < 1 µm. Peak and background counting times were c. 20–40 s. A suite of well-characterized natural

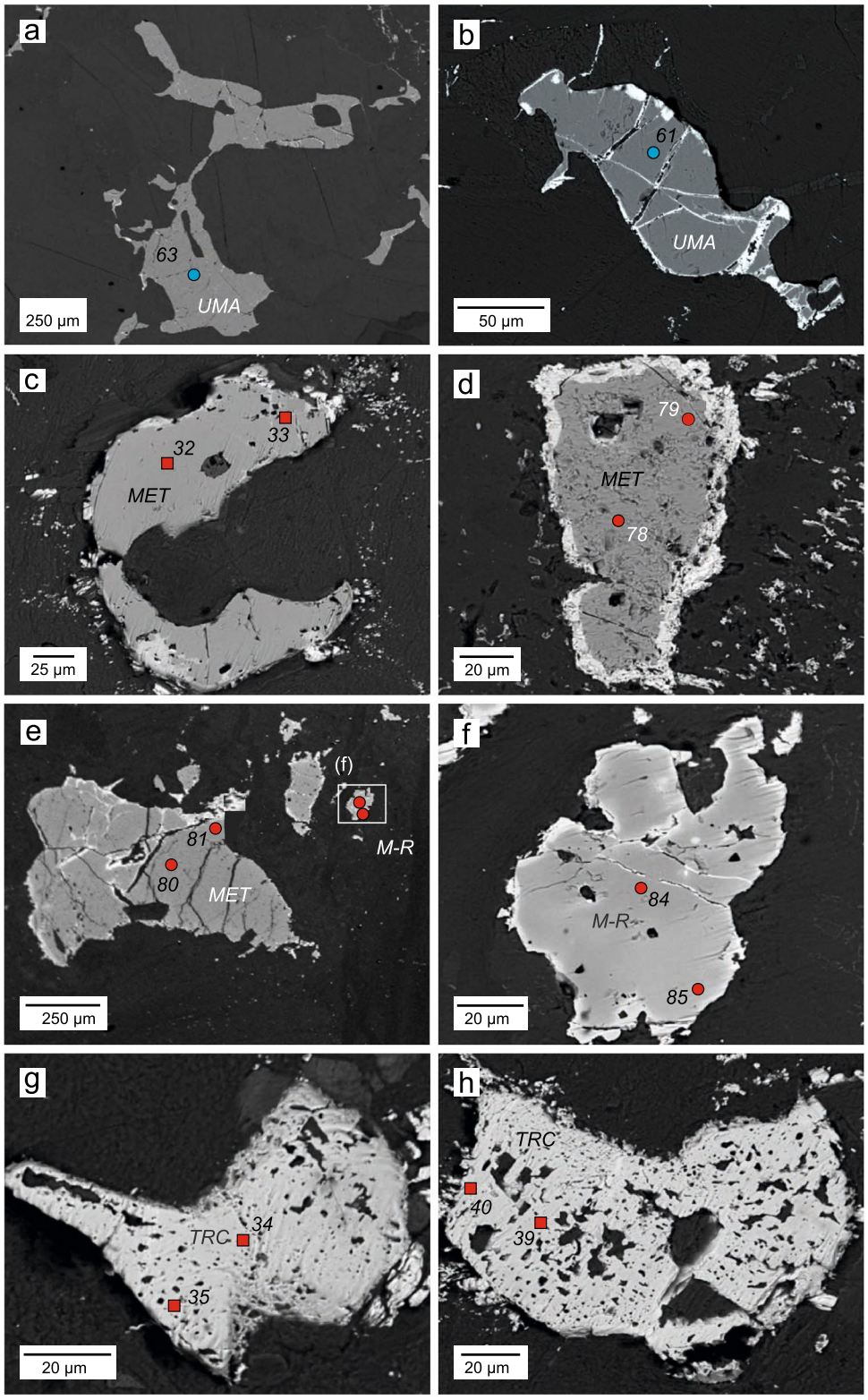

Fig. 3 Representative SEM BSE images of (**a**, **b**) unmetamorphosed, mantle array, (**c**, **d**, **e**) low-Ti metamorphosed, (**f**) high-Ti melt-reacted Cr–spinel and (**g**, **h**) Ti-rich chromite (for definition of these Cr–spinel and chromite types, see Fig. 5 and text) in Expedition 357 Atlantis Massif peridotite. **a**, **b** Unaltered Cr–spinel cores in western Type I serpentinized harzburgite, 71C-1R1-6-10 (spot 63, Cr#, Mg# and TiO_2 of 0.30, 0.74, and 0.09 wt.%; spot 61, Cr#, Mg#, and TiO_2 of 0.30, 0.71 and 0.04 wt.%). **c** Weakly metamorphosed Cr–spinel core and rim in central Type I serpentinized dunite, 76B-3R1-78–82 (spot 32, Cr#, Mg#, and TiO_2 of 0.47, 0.59, and 0.21 wt.%; spot 33, Cr#, Mg# 0.47, 0.54 and 0.22 wt.%). **d** Moderately metamorphosed Cr–spinel core and rim in central Type II melt-impregnated harzburgite, 76B-6R1-65–68 (spot 78, Cr# of 0.38, Mg# of 0.48; spot 79, Cr# 0.38, Mg# of 0.48). **e**, **f** Melt-reacted core and rim in central Type II melt-impregnated harzburgite, 76B-6R1-65-68 (spot 84, Cr#, Mg#, and TiO_2 of 0.43, 0.45, and 0.43 wt.%; spot 85, Cr#, Mg#, and TiO_2 of 0.57, 0.33, and 0.35 wt.%). (g, h) Ti-rich chromite cores and pairs in central Type I serpentinized dunite, 76B-3R1-78-82 (spot 34, Cr#, Mg#, and TiO_2 of 0.90, 0.12, and 0.99 wt.%; spot 35, Cr#, Mg#, and TiO_2 of 0.92, 0.12, and 1.11 wt.%; spot 39, Cr#, Mg#, and TiO_2 of 0.87, 0.14, and 0.78 wt.%; spot 40, Cr#, Mg# and TiO_2 of 0.93, 0.12, and 1.23 wt.%. *MET* metamorphosed, *M-R* melt reacted, *TRC* Ti-rich chromite, *UMA* unmetamorphosed, mantle array

and synthetic minerals and compounds were used as primary and secondary calibration standards. Raw X-ray data were processed using the atomic number and absorption corrections of Pouchou and Pichoir (1991), the characteristic fluorescence correction of Reed (1990), and the continuum fluorescence correction of Springer (1971). The mass absorption coefficients of Heinrich (1987) were used in the calculations. Atomic number and absorption corrections are

from the PAP model of Pouchou and Pichoir (1991) and absorption correction in conjunction with the mass absorption coefficients of Heinrich (1987). Characteristic fluorescence corrections are based on Reed (1990).

Data compilation and manipulation

In the mineral chemistry plots (Figs. 4–13), we compare spinel chemistry data from this study with similar data collected on Atlantis Massif serpentinite from Rouméjon et al. (2018a) and Akizawa et al. (2020). Fe_2O_3/FeO values of spinel are calculated on the basis of stoichiometry (3 cations based on 4 oxygens per formula unit). In our mineral chemistry plots, we use only mineral analyses that yield oxide totals of 98–102 wt.%. Oxygen fugacities and spinel closure temperatures were calculated using the calibrations in Ballhaus et al. (1990, 1991) assuming a constant olivine composition of Fo_{90}, as most samples did not contain olivine due to extensive serpentinization, and the presence of orthopyroxene before serpentinization.. The effect of olivine Fo content on the calculated oxygen fugacities and spinel equilibration temperatures is small, e.g., using Fo_{91} instead of Fo_{90} changes (lowers) fO_2 by 0.26 log unit and closure temperature by ~ 30–70 °C.

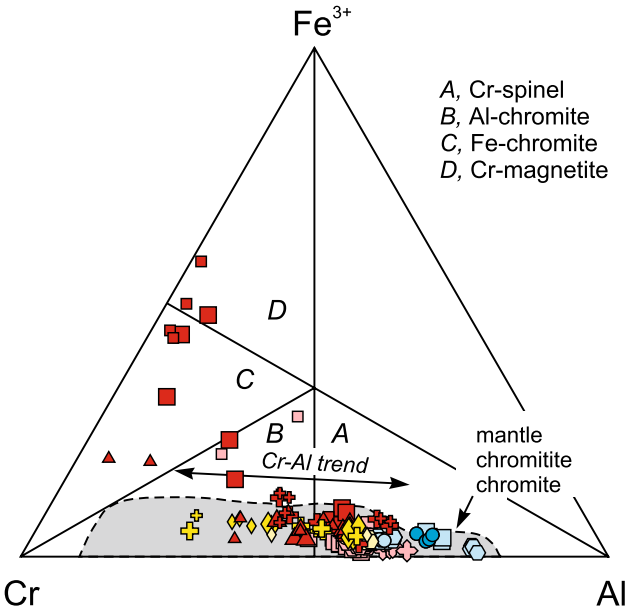

Fig. 4 Trivalent cation plots of Cr–Fe^{3+}–Al of Expedition 357 peridotite spinel on the classification plot of Stevens (1944). The Cr–Al trend is as defined by Barnes and Roeder (2001) and this trend is also manifest as an increase in Fe# ($Fe^{2+}/Fe^{2+}+Mg^{2+}$) with increasing Cr# (Cr/Cr + Al) (not shown). Samples are classified on the basis of macroscopic, microscopic and whole peridotite chemistry (see Whattam et al. 2022 and references therein). The field of mantle chromitite chromite is from Arai and Yurimoto (1994). Symbols are as in Fig. 1d

Results

All peridotite is highly serpentinized, but many have undergone additional alteration processes including mafic melt-impregnation and silica metasomatism (Fruh-Green et al. 2018; Rouméjon et al. 2018a; Akizawa et al. 2018; Whattam et al. 2022). The above forms the foundation for subdivision into three serpentinite types: I, serpentinite, II, melt-impregnated serpentinite, and III, metasomatic serpentinite (Whattam et al. 2022). The effects of silica metasomatism are obvious based on whole-rock geochemistry (e.g., elevated SiO_2) and alteration of orthopyroxene to talc and amphibole (Fruh-Green et al. 2018; Rouméon et al. 2018a; Whattam et al. 2022). Mafic melt-impregnation is recognizable at the scale of core (e.g., Fruh-Green et al. 2018) in some cases; in other situations, melt-impregnation is cryptic and recognizable only by consideration of whole-rock trace element chemistry (Whattam et al. 2022).

Mineral chemistry

We obtained 71 analyses of spinel cores and rims comprising serpentinite of all types and sites (western, central, eastern; Fig. 1d). To investigate the effects of melt-impregnation, silica metasomatism and metamorphism on Expedition 357 peridotites, we specifically targeted Cr–spinel of peridotite that has been subjected to compositional modification beyond serpentinization, i.e., Type II melt-impregnated serpentinite and Type III metasomatized serpentinite, in addition to the ones subjected to serpentinization only (Type I serpentinite). Representative spinel analyses are provided in Table 1 and all spinel analyses are provided in Supplementary Table S1. Including the spinel analyses of Rouméjon et al. (2018a) and Akizawa et al. (2020), the total number considered in this study is 156 points.

Cr–spinel and chromite in Cr–Fe^{3+}–Al space

The spinel classification prism of Stevens (1944) (Fig. 4) shows the distribution of the Atlantis Massif peridotite Cr–spinel and chromite in terms of Cr–Fe^{3+}–Al. Most Cr–spinel from this study and recent studies (Rouméjon et al. 2018a; Akizawa et al. 2020) are Al rich (i.e., plot within the field of Cr–spinel, 52%) with lesser Cr-rich ones (i.e., plot within the field of Al-chromite, 34%), which define a Cr–Al trend (Barnes and Roeder 2001). A subordinate number of spinels (14%) exhibit more Fe^{3+} and classify as Fe–chromite and Cr–magnetite (hereafter, we use the term Ti-rich chromite, for reasons further explained in Sect. 6, to encompass Fe–chromite and Cr–magnetite). Cr/Al is lowest in Cr–spinel of Type I serpentinite of western Site M0071C (0.41–0.46) and highest in Cr–spinel of Type II

Table 1 Chemical compositions of representative spinel of Expedition 357 peridotites from this study

Sample no./name	71C-1R1-6–10	71C-1R1-6–10	71C-1R1-6–10	71C-1R1-6–10	76B-6R1-65–68	76B-6R1-65–68	76B-6R1-65–68	68B-4R1-23–29	69A-9R2-8–12	76B-3R1-78–82	76B-3R1-78–82	76B-6R1-65–68	68B-1R1-10–13	68B-4R1-23–29	76B-3R1-78–82	76B-3R1-78–82	76B-8R1-107.5–112.5	76B-8R1-107.5–112.5
Site	W	W	W	W	C	C	C	E	C	C	C	C	E	E	C	C	C	C
rock type	Ty I serp harz	Ty I serp harz	Ty I serp harz	Ty I serp harz	Ty II melt-impreg harz	Ty II melt-impreg harz	Ty II melt-impreg harz	Ty II melt-impreg harz	Ty I Ca-rich harz	Ty I ser-pent dunite	Ty I ser-pent harz	Ty II melt-impreg harz	Ty III Si-meta-som-atized harz	Ty II melt-impreg harz	Ty I serp-dunite	Ty I serp-dunite	Ty I Ca-rich harz	Ty I Ca-rich harz
Cr–spinel spot	32	33	30	29	60	58	57	14	27	34	35	55	6	15	37	42	65	63
core or rim	core	core	core	core	core	rim	rim	rim	core	core	core	core	core	core	core	rim	core	rim
Cr–spinel type	UMA	UMA	UMA	UMA	M-R	M-R	M-R	M-R	MET	MET	MET	MET	MET	MET	M-R TRC	M-R TRC	MET TRC	MET TRC
wt.%																		
SiO_2	0.03	0.01	0.04	0.01	0.03	0.04	0.00	0.02	0.00	0.01	0.02	0.02	0.00	0.02	0.08	0.11	0.24	0.1
TiO_2	0.09	0.05	0.04	0.06	0.35	0.62	0.68	0.33	0.09	0.21	0.22	0.04	0.06	0.13	1.11	1.23	0.21	0.25
Al_2O_3	41.23	41.27	41.56	39.14	19.42	20.93	19.79	26.61	29.58	28.26	26.88	32.46	30.89	24.11	1.93	1.50	5.88	2.4
Fe_2O_3	2.88	4.03	3.11	4.26	9.93	9.5	9.26	4.43	4.58	5.50	6.77	2.28	3.35	4.93	29.54	33.89	13.58	13.78
FeO	11.02	11.78	12.37	13.00	24.22	23.55	23.33	19.83	16.58	16.23	17.86	16.86	15.06	21.79	28.57	28.82	28.45	28.41
MnO	0.12	0.17	0.15	0.14	0.39	0.36	0.35	0.25	0.22	0.21	0.25	0.24	0.20	0.28	0.49	0.45	0.72	0.92
CaO	0.00	0.01	0.00	0.01	0.00	0.01	0.00	0.01	0.01	0.00	0.01	0.00	0.00	0.01	0.00	0.01	0	0.05
MgO	17.83	17.14	17.09	16.26	6.69	7.87	7.65	10.31	12.87	13.13	11.80	13.06	13.93	8.84	2.20	2.15	2.47	1.84
NiO	0.26	0.24	0.20	0.19	0.11	0.14	0.14	0.23	0.14	0.14	0.17	0.13	0.19	0.16	0.33	0.41	0.08	0.05
Cr_2O_3	26.80	25.06	26.30	27.14	37.80	37.79	38.54	37.39	35.85	36.53	36.00	35.26	36.14	39.89	34.38	30.53	47.57	51.36
Total	100.26	99.76	100.86	100.21	98.94	100.81	99.74	99.41	99.92	100.22	99.98	100.35	99.82	100.16	98.63	99.10	99.2	99.16
FeO/FeO (Tot)	0.81	0.76	0.82	0.77	0.73	0.73	0.74	0.83	0.80	0.77	0.75	0.89	0.83	0.83	0.52	0.49	0.7	0.7
FeO (Tot)	13.61	15.41	15.17	16.83	33.16	32.1	31.66	23.82	20.70	21.18	23.95	18.91	18.07	26.23	55.15	59.32	40.67	40.81
At. prop																		
Si	0.00	0.00	0.00	0.00	0.00	0	0.00	0.00	0.00	0.00	0.00	0.00	0.00	0.00	0.00	0.00	0.01	0
Ti	0.00	0.00	0.00	0.00	0.01	0.01	0.02	0.01	0.00	0.00	0.01	0.00	0.00	0.00	0.03	0.03	0.01	0.01
Al	1.35	1.36	1.36	1.30	0.75	0.79	0.76	0.97	1.04	1.00	0.97	1.13	1.08	0.89	0.08	0.07	0.25	0.1
Fe^{3+}	0.06	0.08	0.06	0.09	0.25	0.23	0.23	0.10	0.10	0.12	0.16	0.05	0.07	0.12	0.83	0.95	0.37	0.38
Cr	0.59	0.55	0.58	0.61	0.98	0.95	0.99	0.91	0.85	0.87	0.87	0.82	0.85	0.99	1.01	0.90	1.35	1.49
Fe^{2+}	0.26	0.28	0.29	0.31	0.67	0.63	0.63	0.51	0.42	0.41	0.46	0.42	0.37	0.57	0.89	0.90	0.86	0.87
Mh	0.00	0.00	0.00	0.00	0.01	0.01	0.01	0.01	0.01	0.01	0.01	0.01	0.01	0.01	0.02	0.01	0.02	0.03
Ca	0.00	0.00	0.00	0.00	0.00	0	0.00	0.00	0.00	0.00	0.00	0.00	0.00	0.00	0.00	0.00	0	0
Mg	0.74	0.71	0.71	0.68	0.33	0.37	0.37	0.48	0.57	0.59	0.54	0.57	0.62	0.41	0.12	0.12	0.13	0.1
Ni	0.01	0.01	0.00	0.00	0.00	0	0.00	0.01	0.00	0.00	0.00	0.00	0.00	0.00	0.01	0.01	0	0
Total	3.01	2.99	3.00	2.99	3.00	2.99	3.01	3.00	2.99	3.00	3.02	3.00	3.00	2.99	2.99	2.99	3	2.98
Cr#	0.30	0.29	0.30	0.32	0.57	0.55	0.57	0.49	0.45	0.46	0.47	0.42	0.44	0.53	0.92	0.93	0.84	0.93
Mg#	0.74	0.72	0.71	0.69	0.33	0.37	0.37	0.48	0.58	0.59	0.54	0.58	0.62	0.42	0.12	0.12	0.13	0.1
$Fe^{3+}/(Cr+Al+Fe^{3+})$	0.03	0.04	0.03	0.05	0.12	0.12	0.11	0.05	0.05	0.06	0.08	0.03	0.04	0.06	0.43	0.50	0.19	0.19

Table 1 (continued)

Sample no./name	71C-1R1-6–10	71C-1R1-6–10	71C-1R1-6–10	76B-6R1-65–68	76B-6R1-65–68	76B-6R1-65–68	68B-4R1-23–29	69A-9R2-8–12	76B-3R1-78–82	76B-3R1-78–82	76B-6R1-65–68	68B-1R1-10–13	68B-4R1-23–29	76B-3R1-78–82	76B-3R1-78–82	76B-8R1-107.5–112.5	76B-8R1-107.5–112.5
Fe/(Fe-tot)	0.81	0.76	0.82	0.77	0.73	0.73	0.74	0.83	0.80	0.77	0.75	0.89	0.83	0.83	0.52	0.49	0.7	0.7
F	12.08	11.6	11.89	12.53														
T closure (°C)	849.19	792.81	762.71	750.96	544.03	575.42	581.54	596.37	681.24	719.15	672.13	636.92	722.6	561.12	566	581.39	480.23	469.84
DQMF (Tclosure)	0.16	0.88	0.47	1.03	2.77	2.64	2.59	1.31	1.17	1.4	1.87	0.09	0.54	1.51	4.72	4.97	3.28	3.31
Olivine Fo	90.95	90.95	90.95	90.95	90.95	90.95	90.95	90.95	90.95	90.95	90.95	90.95	90.95	90.95	90.95	90.95	90.95	90.95

UMA unmetamorphosed mantle array, *MET* metamorphosed, *M-R* melt reacted, *TRC* Ti-rich chromite

melt-impregnated serpentinite of eastern Site M0068B. No significant compositional differences are apparent between Cr–spinel cores and rims.

On the basis of Cr# vs. Mg# and Cr# vs. TiO_2 (Fig. 5), Cr–spinel and chromite of this study are subdivided into those that are (i) unmetamorphosed; (ii) metamorphosed; and (iii) melt reacted (further explanation for this subdivision is provided in the next section). Type I serpentinite of the western site is unmetamorphosed, whereas many Cr–spinel grains with higher Cr/Al from the central and eastern site serpentinite are consistent with being metamorphosed to varying degrees, e.g., those with higher Cr/Al record higher temperature metamorphism relative to ones with lower Cr/Al. Other Cr–spinel and Ti-rich chromite (those which plot within the fields of Fe–chromite and Cr–magnetite on the basis of nomenclature of Stevens 1944) are consistent with having been melt reacted, for reasons explained below.

Discrimination of Cr–spinel into unmetamorphosed, melt reacted and metamorphosed

To discriminate unmetamorphosed Cr–spinel from the ones subjected to modification by metamorphism and/or melt–rock reaction, we first plot all Atlantis Massif Cr–spinel from this study and the studies of Rouméjon et al. (2018a) and Akizawa et al. (2020) in plots of Cr# vs. Mg# and Cr# vs. TiO_2 (Fig. 5). The rationale for plotting these values is that in the Cr# vs. Mg# space, unmetamorphosed Cr–spinel will plot within the mantle array (Dick and Bullen, 1984), whereas the ones subjected to modification via melt-impregnation or metamorphism will instead plot outside the the mantle array (on Fig. 5a, b); subsequent plotting of Cr–spinel in Cr# vs. TiO_2 space allows for discrimination of melt-reacted spinel with high TiO_2 from (low TiO_2) metamorphosed spinel. As shown in Cr# vs. Mg# space (Fig. 5a, b), the vast majority of Cr–spinel that plots in the mantle array is from the western site Type I fluid–rock dominated serpentinites and, indeed, all western site Type I serpentinite Cr–spinel plot within the mantle array. In contrast, the vast majority of Cr–spinel of the central and eastern site melt-dominated serpentinites plots to the right of the mantle array indicative of low degree of metamorphism or to the upper right of the array indicative of higher degrees of metamorphism. When Atlantis Massif Cr–spinel is plotted in the Cr# vs. TiO_2 space (Figs. 5c, d), discrimination between low-Ti metamorphosed Cr–spinel and high-Ti, melt-reacted Cr–spinel is clear with those with > 0.25 wt.% TiO_2 defining the ones as melt reacted from the ones with < 0.25 wt.% TiO_2, which are best described as low-Ti metamorphosed Cr–spinel. Melt-reacted spinel comprises up to 0.68 wt.% TiO_2 and fall within the range of TiO_2 of Atlantis Massif basalt

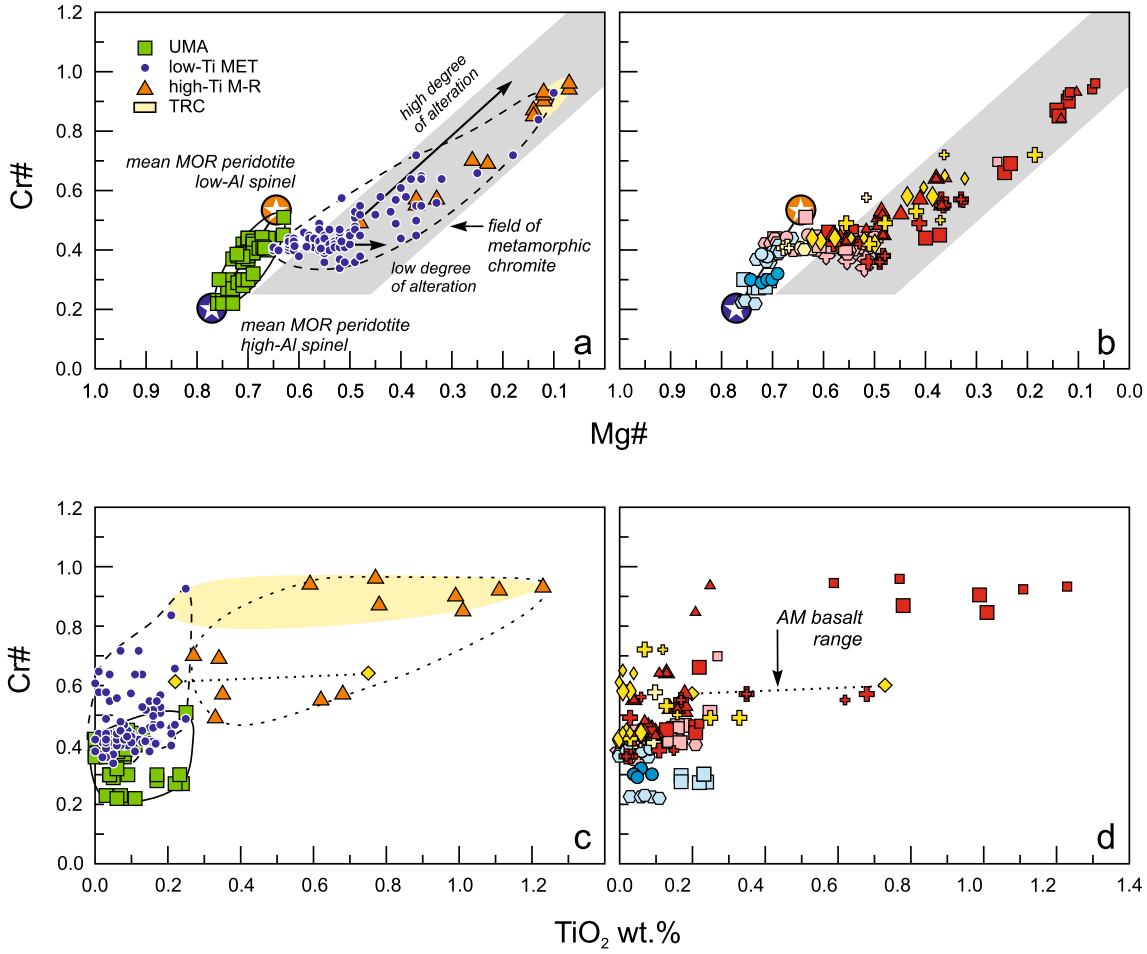

Fig. 5 **a**, **b** Cr# vs. Mg# and **c**, **d** Cr# vs. TiO_2 of Cr–spinel of Atlantis Massif serpentinitized peridotites from this study and the studies of Rouméjon et al. (2018a, b) and Akizawa et al. (2020). **a**, **c** Our interpretation of **b** and **d** as unmetamorphosed mantle array (UMA, those plotting within the mantle array), low-Ti metamorphic (MET), and high-Ti (>0.25 wt.% TiO_2) melt reacted (M-R). In (**a**, **b**), mean MOR peridotite low-Al and high-Al spinel are from Dick and Bullen (1984); a line connecting them can be considered as representative of an unaltered, primary MOR peridotite Cr–spinel trend. Also in (**a**, **b**) is the field of metamorphic chromite, which is based on Evans and Frost (1975). Symbols in Fig. 5b and 5d are as in Fig. 1d. Other abbreviation: *TRC* Ti-rich chromite

(unpublished data, first author) whereas melt-reacted chromite comprises up to 1.23 wt% TiO_2.

These two plots of Cr# vs. Mg# and Cr# vs. TiO_2 also show a clear relationship between microscopic and macroscopic observations and whole-rock chemistry interpretations (Whattam et al. 2022) and Cr–spinel chemistry. Whereas Cr–spinel of the Type I fluid-dominated serpentinites of the western sites, which show no evidence of melt-impregnation or melt–rock reaction all plot within the mantle array, most Cr–spinel of serpentinite from the central and eastern sites, which comprise high percentages of Types II and III melt-impregnated and metasomatized peridotite, instead show clear evidence of having been modified by metamorphism and/or melt–rock interaction.

Petrogenesis

Estimates of degree of melt extraction

Moderate to high degrees of melt extraction are evident in low whole-rock Al2O3/SiO2 and low concentrations of Al2O3, CaO, and incompatible elements of Atlantis Massif peridotites (Früh-Green et al., 2018; Whattam et al., 2022). Relatedly, results of whole-rock chemistry petrological modeling suggest a high degree (a maximum of 19–21%) of partial melting for the most depleted peridotite, with no significant variation between sites (Whattam et al. 2022).

Here, we calculate and provide the exact degrees of melt extraction experienced by Atlantis Massif peridotites based on spinel Cr# for comparison with results obtained via whole-rock chemistry by Whattam et al. (2022).

Based on moderately incompatible HREE in abyssal peridotite clinopyroxene showing high correlation with Cr# of coexisting spinel, Hellebrand et al. (2001) developed an empirical equation that describes the extent of fractional melting (F) of mantle peridotite as a function of spinel Cr#. Applying this equation (F = 10ln(Cr#) + 24) to unmetamorphosed, mantle array (UMA) Atlantis Massif peridotite spinel from this study and those of Rouméjon et al. (2018a) and Akizawa et al. (2020) ($n = 49$) yields estimates of F of 9–18% melting (Table 1, Supplementary Table 1), which falls just below the lower limit of maximum F deduced from whole-rock HREE contents (19–21%, Whattam et al., 2022).

Fugacity and thermometry

We calculated oxygen fugacity using the olivine–orthopyroxene–spinel barometer of Ballhaus et al. (1990, 1991), where $\Delta\log(fO_2)$FMQ represents a log unit difference in oxygen fugacity from the fayalite–magnetite–quartz (FMQ) buffer assuming a pressure of 1.5 GPa within the spinel lherzolite field. On a plot of $\Delta\log(fO_2)$FMQ vs. spinel Cr# (Fig. 6a), primary unmetamorphosed mantle array Cr–spinel plots mostly within the field of abyssal peridotite with minor overlap into the abyssal dunite field recording a range of $\Delta\log(fO_2)$FMQ of − 1.7 to + 1.0.

We calculate spinel–olivine temperatures based on Ballaus (1997) olivine–spinel Fe–Mg exchange. For slow cooling rocks, these calculated temperatures represent closure temperatures and not the temperature of the ambient mantle prior to exhumation. Closure temperatures, i.e., temperatures at which observable diffusion stops, provide significant evidence on the cooling and tectonic history of the studied rocks. On average, abyssal peridotite tends to have higher equilibration temperatures than Alpine peridotite, which Henry and Medaris (1980) and Dick and Fisher (1984) ascribed to faster cooling of the former as a result of seawater influx. The lower temperatures of forearc peridotite may be related to diffusional equilibrium being assisted by slab-derived fluids (e.g., Parkinson and Pearce 1996).

As Cr–spinel compositions have not been affected by serpentinization (Fig. 5), Mg–Fe systematics in spinel are due to exchange with olivine. Assuming olivine Fo_{90}, we calculate temperatures for each spinel. Temperatures calculated from olivine–spinel Mg–Fe exchange thermometry (Ballhaus et al. 1991) yield a mean closure of 808 ± 39 ºC with a range from 708 to 884 °C (Fig. 6b) for Expedition 357 Type I serpentinites, which fall within the mid-range of those obtained for abyssal peridotites of about 625–1000 °C and a mean near 800 °C (see Parkinson and Pearce 1996).

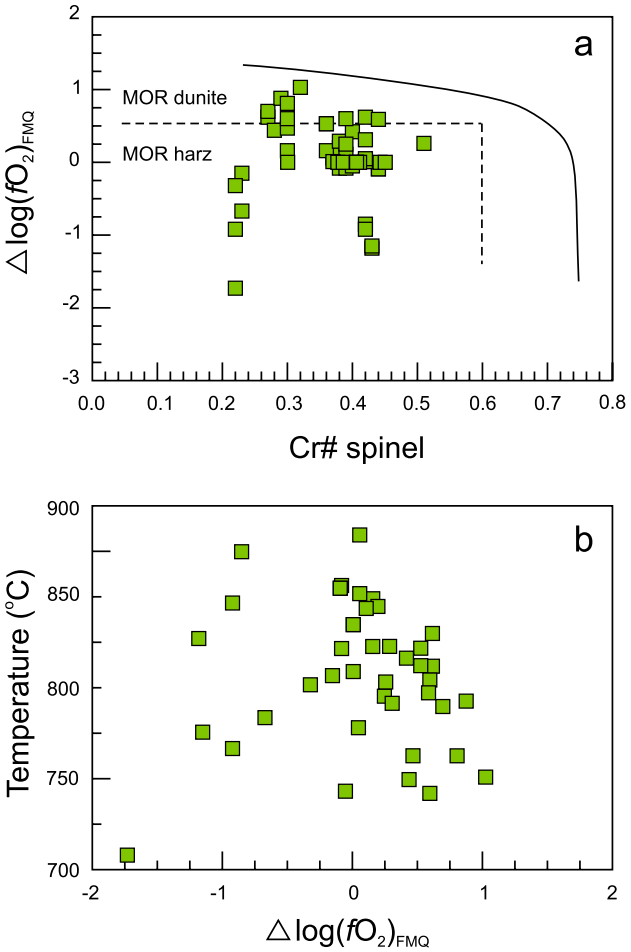

Fig. 6 **a** $\Delta\log(fO_2)_{FMQ}$ vs. Cr# spinel and **b** temperature vs. $\Delta\log(fO_2)_{FMQ}$ of unmetamorphosed mantle array Cr–spinel. Fields of MOR harzburgite and MOR dunite are from Dare et al. 2009

Discussion

Evidence for melt–rock interaction (melt-impregnation)

Whole-rock incompatible element abundances and HFSE/LREE trends provide evidence of mafic melt-impregnation in Expedition 357 Atlantis Massif peridotite, which exhibits macroscopic evidence of melt-impregnation (Whattam et al. 2022). Below, we provide evidence of melt-impregnation in Expedition 357 peridotite via Cr–spinel and chromite TiO_2 abundances and olivine compositions.

Cr–spinel TiO_2 abundances and oxidation

Significant features of Atlantis Massif melt-reacted Cr–spinel and chromite are very low Mg#, high Cr# and TiO_2 (Fig. 5), and the highest-Ti chromite is from Type II melt–rock dominated central dunite of Site 76B.

If a peridotite is melt impregnated, the spinel Ti contents preserve a record of the nature of the impregnating melt as opposed to the primary composition of the host peridotite (Dick and Bullen 1984; Cannat et al. 1990); because impregnating mafic melts are generally richer in Ti relative to unaltered peridotite, re-equilibrated spinel from melt-impregnation should have higher Ti concentrations than unaltered peridotites (Pearce et al., 2000). In spinel Cr# vs. TiO_2 space (Figs. 5c, d), Expedition 357 Type II melt-impregnated serpentinite of the central and eastern sites has Cr–spinel with ~ 0.3–0.7 wt.% TiO_2, higher than other spinel TiO_2 in Expedition 357 serpentinite and within the range of an eastern site basalt (~ 0.2–0.7 wt.% TiO_2) (sample 68-B-7R1-29-33, Whattam unpublished data) confirming their mafic melt-impregnated nature.

Perhaps the most salient observation of Fig. 5 is that the highest TiO_2 concentrations belong to chromite of (central) dunite. Studies of abyssal and ophiolitic peridotite have shown that the lithospheric mantle compositional variability at extensional settings is caused chiefly by reactive percolation of rising melts in the thermal boundary layer and subsequent melt–rock interaction as recorded by lithospheric peridotite. As summarized by Kelemen et al. (1995b), two main origins for the formation of dunite have been proposed. In the first case, cumulative dunite is magmatic and formed by fractionation of olivine from a mafic melt (e.g., Nicolas and Jackson 1982; Takahashi 1992). In the second case, replacive dunite forms as the result of melt–rock processes and the product of reaction between a pyroxene-bearing host rock (i.e., harzburgite) and an olivine-saturated magma that causes orthopyroxene dissolution in the host peridotite and commonly the crystallization of secondary (replacive) olivine (Quick 1981; Berger and Vannier 1984; Kelemen 1990; Bodinier et al. 1991; Kelemen et al. 1992, 1995a, b). Collective evidence points to the second origin as being most likely in most cases (Kelemen et al. 1995a, b). However, it is important to note that these above two processes are not necessarily contradictory, i.e., melt–peridotite reaction should also entail olivine precipitation from the olivine-oversaturated magma and release of heat to promote reaction. At any rate, in the case of the Atlantis Massif, the second interpretation is what was proposed by Whattam et al. (2022) for eastern melt-impregnated peridotite 68B-4R1-23-29 (Fig. 2e). With respect to dunite Ti-rich chromite TiO_2 abundances (Arai and Matsukage 1996), these range to the highest values (from 0.6 to 1.2 wt.% TiO_2).

Differences in oxidation between unmetamorposed mantle array, metamorphosed and melt-reacted spinel

Another manifestation of melt–peridotite interaction is the highly oxidized nature of melt-affected peridotite (e.g., Parkinson and Pearce 1996). Anomalously high fugacity is recorded by melt-reacted Cr–spinel and Ti-rich chromite and a prominent trend from unmetamorphosed and unreacted Cr–spinel to the latter is evident (Fig. 7). Whereas the metamorphic spinel records moderate oxidation, the melt-reacted Cr–spinel and chromite record extreme oxidation. Unmetamorphosed and metamorphosed Cr–spinel record a maximum $Fe^{3+}/(Fe^{3+}+Cr+Al)$ of ~ 0.05 and 0.2, respectively, but the melt-reacted Cr–spinel and chromite record $Fe^{3+}/(Fe^{3+}+Cr+Al)$ of up to nearly 0.6. Interestingly, the vast majority of melt-reacted spinel is from (central) dunite (9 of the 13 melt-reacted spinel and chromite are from central Type II melt-dominated dunite). Indeed, the 'most' melt-reacted Cr–spinel and chromite are of Atlantis Massif dunite and record Cr# up > 0.95 and the highest $Fe^{3+}/(Fe^{3+}+Cr+Al)$ of all samples (Fig. 7).

Effect of melt–rock interaction on olivine Fo

Melt–peridotite interaction, as recorded by some central and eastern site melt-impregnated peridotite (Fruh-Green et al. 2018; Whattam et al. 2022), are consistent with dissolution of orthopyroxene by infiltrating olivine-saturated melts that drove subsequent olivine re-crystallization and the addition of cumulus olivine from the (probably) olivine-oversaturated melt (Arai and Matsukage 1996; Kelemen 1990; Kelemen et al. 1995a, b, 1997; Quick 1981; Suhr et al. 2003).

A significant trend recorded by Atlantis Massif peridotite olivine also provides further critical evidence of melt–rock interaction. An olivine NiO vs. olivine Fo plot (Fig. 8) shows displacement of olivine compositions of serpentinite from central Sites M0072 and M0076 (Rouméjon et al. 2018a) to lower, 'non-mantle' olivine Fo (minimum of $Fo_{86.5}$) at relatively constant NiO concentrations. The olivine

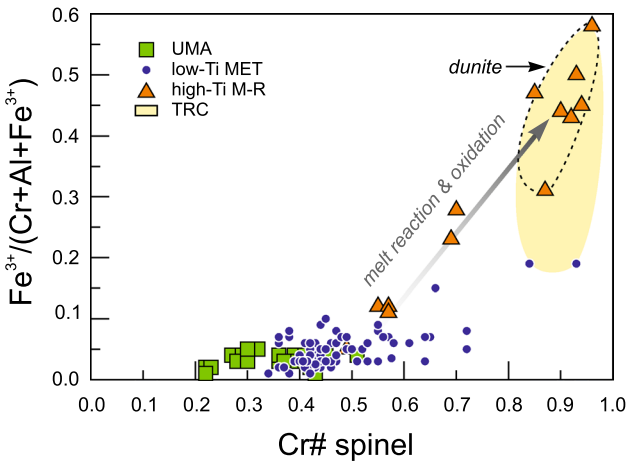

Fig. 7 $Fe^{3+}/(Cr+Al+Fe^{3+})$ vs. Cr# spinel of Cr–spinel and Ti-rich chromite. *UMA* unmetamorphosed mantle array, *MET* metamorphic, *M-R* melt reacted, *TRC* Ti-rich chromite

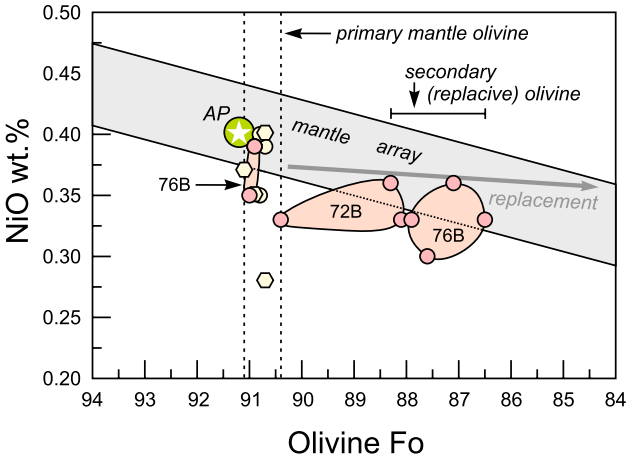

Fig. 8 Olivine NiO vs. olivine forsterite content. The olivine replacement trend represents open system melting between harzburgite and infiltrating melts of evolved composition and is from Niida (1997). Atlantis Massif peridotite olivine are from Roumejon et al. (2018a, eastern and central harzburgites) and Akizawa et al. (2020, eastern peridotites). Abyssal MAR peridotite (AP, $Fo_{91.2}$) is from Shibata and Thompson (1986) and the mantle array is from Takahashi et al. (1987). Symbols are as in Fig. 1d.

displacement trend parallels the 'replacive' trend (Fig. 8; Niida 1997) of olivine that forms due to interaction of secondary infiltrating melts with refractory harzburgitic residue. Thus, some olivine grains of central Sites M0072 and M0076 peridotites are consistent with a secondary, replacive origin. In such a scenario, these peridotites represent 'reactive' peridotite that interacted with secondary melts that also impregnated the peridotite. Furthermore, central Site M0072 serpentinite is considered as 'cryptically' melt impregnated (Whattam et al. 2022). Along with the elevated TiO_2 abundances in melt-impregnated peridotite spinel, the low olivine Fo is clear evidence of melt–peridotite reactions resulting in recrystallization of olivine from impregnating melts.

Evidence of sub-greenschist to lower amphibolite metamorphism

Multiple generations of amphibole have been observed in Atlantis Massif gabbro and have been interpreted to represent retrogressive alteration from amphibolite to greenschist facies conditions during exhumation (Schroeder and John 2004; Boschi et al. 2006a). However, to our knowledge, greenschist facies metamorphism has not yet been documented in Atlantis Massif peridotites.

Peridotite Cr–spinel compositions are commonly used to determine aspects of petrogenesis, i.e., degrees of partial melting, nature of the source, and tectonic setting (e.g., Irvine 1967; Dick and Bullen 1984; Barnes and Roeder 2001; Kametsky et al. 2001; De Hoog et al. 2011). In many cases where peridotite is highly serpentinized, as in the case of the Atlantis Massif, Cr–spinel commonly represents the only identifiable phase that retains the primary characteristics. Nonetheless, Cr–spinel is also subject to alteration and many studies have focused on and described the effects of hydrothermal alteration during serpentinization and metamorphism of primary Cr–spinel (e.g., Evans and Frost 1975; Kimball 1990; Burkhard 1993; Absalov 1998; Arai et al. 2006; Säntii et al. 2006; Khalil and El-Makky 2009; Merlini et al. 2009; Aswad et al. 2011; Gargiulo et al. 2013; Saumur and Hattori 2013; Barra et al. 2014; Bhat et al. 2019; Khedr and Arai 2013; Khedr et al. 2022). Of relevance to this study is the modification of Cr–spinel compositions during melt–rock interaction and metamorphism. A noteworthy feature of common alteration of Cr–spinel is an increase in Fe^{3+} and Fe^{2+} contents at the expense of Al and Mg, respectively, without a major change in Cr_2O_3 (e.g., Barnes and Roeder 2001), which results in high Fe and high Cr spinel with a high magnetite component (see Fig. 4). High-Fe spinel is informally known in the literature as 'ferritchromite' or 'ferritchromit' (Spangenberg (1943), and as cited by, among others, Evans and Frost (1975) and Gonzalez-Jiminez et al. (2009)). For simplicity and because of high TiO_2 contents, we use 'high-Ti chromite' to include those that plot as Fe–chromite and Cr–magnetite on the Cr–Fe^{3+}–Al ternary classification (Fig. 4) of Stevens (1944). Merlini et al. (2009) have described a hydration and oxidation reaction of chromite + antigorite to Fe–chromite + Cr–chlorite as a result of intense metamorphic alteration at temperatures greater than 300 °C.

In Fig. 4, we show that almost all Cr–spinel compositions of Expedition 357 serpentinite fall within the field of mantle chromite. The primary, unmetamorphosed mantle array Cr–spinel of the western peridotite (see Fig. 5) plots further to the right with higher Al content than Cr–spinel of serpentinites of other sites. On a plot of spinel Cr# vs. Mg# (Fig. 5), we show that compositional modification of almost all Expedition 357 serpentinite Cr–spinel, apart from those of the western Type I serpentinized peridotites, is readily apparent. In the spinel Cr# vs. Mg# space, unaltered MOR peridotite–spinel defines a trend of increasing Cr# (between ~ 0.13–0.57) with a corresponding modest decrease in Mg# (from ~ 0.80–0.54) (a line connecting mean peridotite high-Al spinel and mean peridotite low-Al spinel can be considered as representative of an unaltered Cr–spinel Cr–Al trend; Fig. 5). This effect is also visible in the closure temperatures of spinel. Whereas unmetamorphosed spinel has closure temperatures > 800 °C (Fig. 6), consistent with rapid cooling during exhumation and therefore preserving temperatures close to peak temperatures, the metamorphosed spinel preserves lower cooling temperatures, consistent with reheating due to melt emplacement and equilibration to lower, metamorphic temperatures (see "Metamorphic closure temperatures").

A horizontal trend to the outside and to the right of the MOR peridotite array (on Fig. 5a, b), i.e., a modest decrease in Mg#, but at constant Cr#, is consistent with relatively low degrees of metamorphism (Säntii et al. 2006). A decrease in Mg# along with a corresponding steep increase in Cr# (Evans and Frost 1975), in contrast, is consistent with higher degrees of metamorphism. Barnes (2000) has suggested that significant Al loss from chromite cores (and hence an increase in Cr#) at temperatures greater than 550 °C to be the result of equilibration with fluids in equilibrium with chlorite.

It is clear by virtue of the horizontal trend in Fig. 5 that the central and eastern site peridotites have been subjected to relatively low degrees of metamorphism. A subordinate number of Cr–spinel of the central and eastern site serpentinite has been subjected to higher degrees of metamorphism by virtue of an increase in Cr# and a concomitant decrease in Mg#. It thus appears that Cr–Al exchange has occurred in addition to the exchange of Mg and Fe^{2+} (between olivine and spinel). In the case of Cr–Al exchange, significant Al loss from chromite cores above 550 °C can be due to equilibration with fluids in equilibrium with chlorite (Barnes, 2000), which may be the case for some Atlantis Massif peridotites.

Decreasing Cr–spinel Mg# at constant Cr# (i.e., relatively low degree of alteration as indicated by the horizontal arrow on Fig. 5) is the consequence of exchange of Mg and Fe^{2+} between Cr–spinel and coexisting silicate minerals, particularly olivine, through the reaction $Mg_{spinel} + Fe^{2+}{}_{olivine} = Mg_{olivine} + Fe^{2+}{}_{spinel}$ (e.g., Barnes, 2000). In contrast to primary, unmetamorphosed mantle array Cr–spinel from western site M0071 serpentinite, which plots within the MOR abyssal peridotite array (Fig. 5) and exhibits a primary trend as explained above for unaltered MOR abyssal peridotite, most central and eastern site serpentinite Cr–spinel shifts away from the MOR peridotite field to higher Cr# indicative of Mg–Fe exchange and Fe^{2+} addition to Cr–spinel, resulting in lower Mg#.

Metamorphism as recorded by Cr–spinel Cr–Al– Fe^{3+} relations and Cr#, Mg#, Fe^{3+} and MnO abundances

We plot Atlantis Massif serpentine Cr–spinel on the Cr–Fe^{3+}–Al diagram spinel classification prism of Stevens (1944) in Fig. 4 to show the distribution of Atlantis Massif peridotite Cr–spinel and chromite in terms of Cr–Fe^{3+}–Al relations. In Fig. 9, we again plot Cr–spinel in Cr–Fe^{3+}–Al space but with superimposed fields of greenschist and lower and upper amphibolite facies metamorphism (Evans and Frost 1975; Suita and Strieder 1996). Figure 9 shows that approximately half of the Cr–spinels, constrained as metamorphic on the basis of Cr–spinel Cr# vs. Mg# (Fig. 5a, b), plot within the fields of greenschist to lower amphibolite facies metamorphism, with the vast majority plotting within the latter field.

For comparison with Fig. 9 and because the relative grade of metamorphism (i.e., greenschist vs. amphibolite facies) is not apparent on Fig. 5, we compare Mg# vs. Cr# again, and Mg# vs. $Fe^{3+}/Cr + Al + Fe^{3+}$ and Mg# vs. MnO, respectively, with compositional fields of metamorphosed spinel of known metamorphic grade (Barnes, 2000) in Fig. 10. This allows us to determine the extent of Fe^{2+}, Fe^{3+}, and MnO addition and whether metamorphic temperatures were

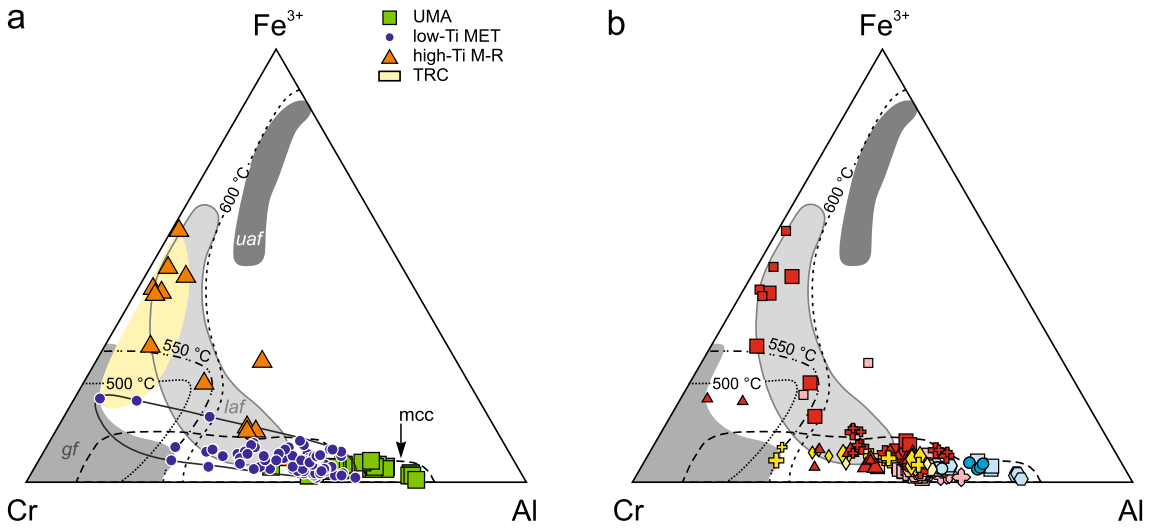

Fig. 9 Trivalent cation plots of Cr–Fe^{3+}–Al of Expedition 357 peridotite spinel as in Fig. 4 but with fields of greenschist facies and lower and upper amphibolite facies (gf, laf, uaf) metamorphism of Evans and Frost (1975) and Suita and Streider (1996). The mantle chromitite chromite (mcc) field is as referenced in Fig. 4 caption. Symbols in b are as in Fig. 1d

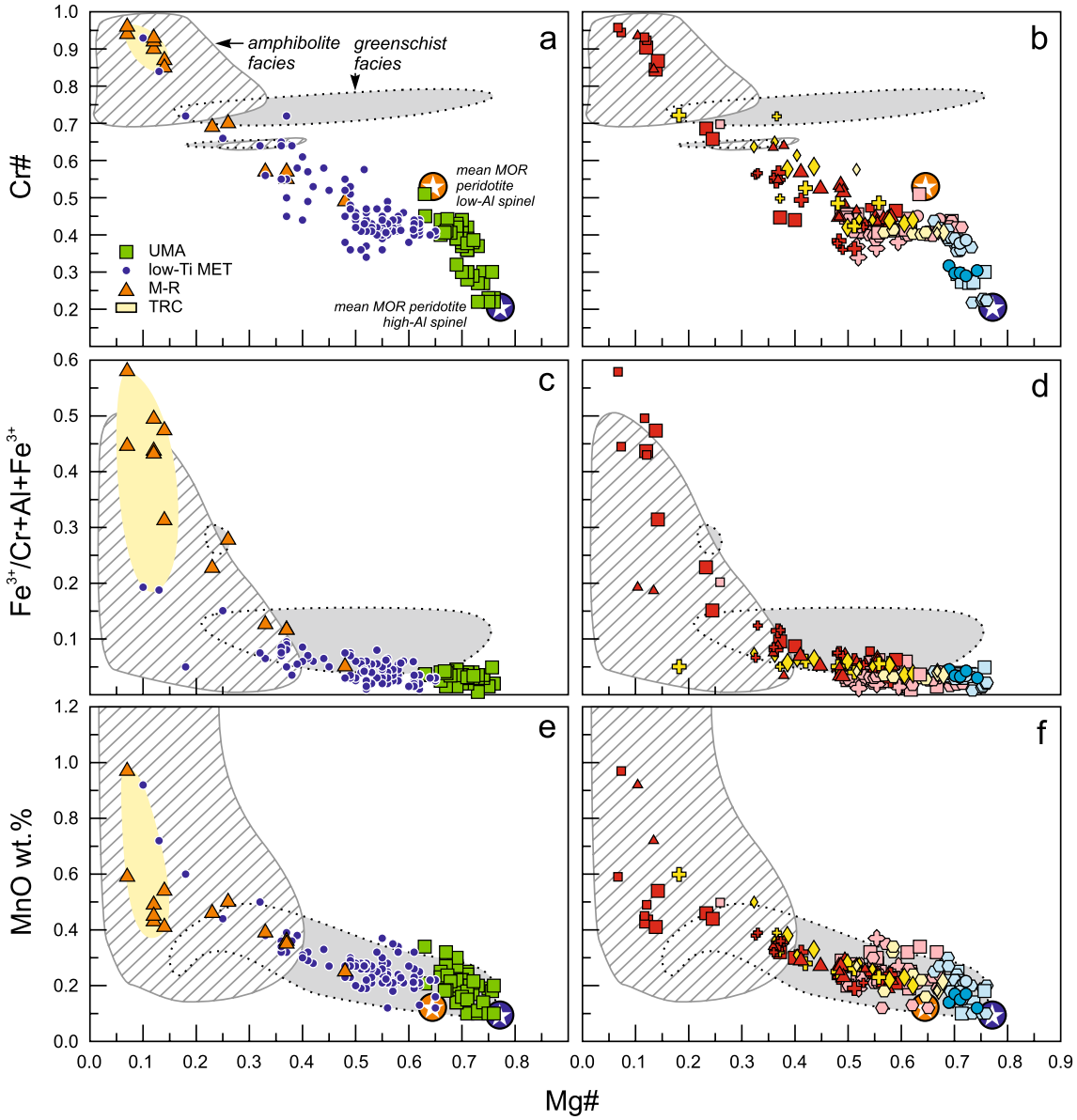

Fig. 10 **a**, **b** Cr# vs. Mg#, **c**, **d** $Fe^{3+}/Cr+Al+Fe^{3+}*100$ vs. Mg#, and **e**, **f** MnO vs. Mg#* of Expedition 357 peridotite Cr–spinel and chromite. **a**, **c**, **e** Our interpretation of Cr–spinel and chromite as unmetamorphosed, metamorphosed and melt reacted (see Fig. 5 and text). The composition fields for Cr–spinel in greenschist and amphibolites facies is for Cr–spinel of metamorphosed komatiites from Barnes (2000) and the greenschist facies does not include those of altered greenschist (see Barnes 2000). The means for MOR peridotite low-Al and high-Al spinel are as referenced in Fig. 5. Symbols in **b**, **d**, **f** are as in Fig. 1d. *UMA* unmetamorphosed mantle array, *MET* metamorphic, *M-R* melt reacted, *TRC* Ti-rich chromite

consistent with greenschist or amphibolite facies metamorphism or conditions of lower temperature (< 300 °C).

Plots of Mg# vs. Cr#, Mg# vs. $Fe^{3+}/Cr+Al+Fe^{3+}$, and Mg# vs. MnO with superimposed fields of amphibolite facies and greenschist facies metamorphism of Cr–spinel (Fig. 10) suggest that metamorphism of central and eastern site peridotite Cr–spinel was mostly low grade (sub-greenschist, < 300 °C) to greenschist, but possibly reaching lower amphibolite facies at ~ 500–600 °C. However, it is important to highlight that closure temperatures calculated for Atlantis Massif serpentinite metamorphic spinel record a higher mean of 610 ºC and much higher upper temperature limit (~ 740ºC) than those suggested in Fig. 9 (see next section). It is also important to emphasize that Cr–spinel ($n = 45$) of the western Type I serpentinite from our study and the study of Akizawa et al. (2020) record no evidence of metamorphism (i.e., lowering of Mg# due to Mg-Fe exchange with olivine) apart from MnO addition for many unmetamorphosed mantle array Cr–spinel from the studies of Rouméjon et al. (2018a) and Ishikawa et al. (2020) which plot within the

greenschist facies field (Figs. 10e, f). We note, however, that the mean MOR peridotite low-Al spinel also plots within the greenschist facies field and the mean MOR peridotite high Al–spinel (Dick and Bullen 1984) of the mantle array plots (just) on the cusp of the greenschist facies field (Fig. 10e, f). Thus, we are uncertain as to the accuracy of the greenschist facies field for Cr–spinel in the MnO vs. Mg# space.

Metamorphic closure temperatures

The mean closure temperature of unmetamorphosed, mantle array Cr–spinel is 808 ± 39 ºC (Fig. 6). It is intriguing that temperatures recorded by the metamorphic Cr–spinel ($n = 106$) yield closure temperatures of 440–737 ºC (mean of 609 ± 64 ºC) (Fig. 11), which are close to and appear to be a record of the metamorphic overprint, i.e., amphibolite and greenschist facies metamorphism at temperatures in the range of ~ 300–700 ºC. We interpret the cooler temperatures for the metamorphic spinel to reflect reheating by infiltrating mafic melts (Fig. 11, see also see next section).

Link between melt-impregnation processes and metamorphism and possible causes of greenschist to amphibolite facies metamorphism

Evidence from Cr–spinel

As mentioned in "Introduction", several generations of amphibole have been observed in Atlantis Massif gabbros interpreted to represent retrogressive alteration from amphibolite to greenschist facies conditions during exhumation (Schroeder and John 2004; Boschi et al. 2006a). Results from this study, however, document a relationship between melt-impregnation and the grade of metamorphism. An important observation from this study is that the only samples that record greenschist to lower amphibolite facies metamorphism as preserved in serpentinite Cr–spinel and chromite (Figs. 9, 10) are from the central and eastern sites that record extensive evidence of mafic melt-impregnation. Apart from perhaps minor addition of MnO (see " Metamorphism as recorded by Cr–spinel Cr–Al-Fe^{3+} relations and Cr#, Mg#, Fe^{3+} and MnO abundances"), there is no evidence of metamorphism in the western site peridotites and this site is the only one that recorded negligible melt-impregnation (Whattam et al. 2022). These observations may instead suggest that greenschist to lower amphibolite facies metamorphism recorded in the central and eastern site serpentinites is the result of localized contact metamorphism from emplacement of diapirs responsible for injection of mafic melt impregnates. Based on the pattern of metamorphism and melt-impregnation documented in Expedition 357 peridotites, it thus appears that melt-impregnation and subsequent metamorphism were focused beneath the central and eastern sites. Further work is needed on serpentinite, which record greenschist to amphibolite facies metamorphism to document further mineralogical evidence of this metamorphic event.

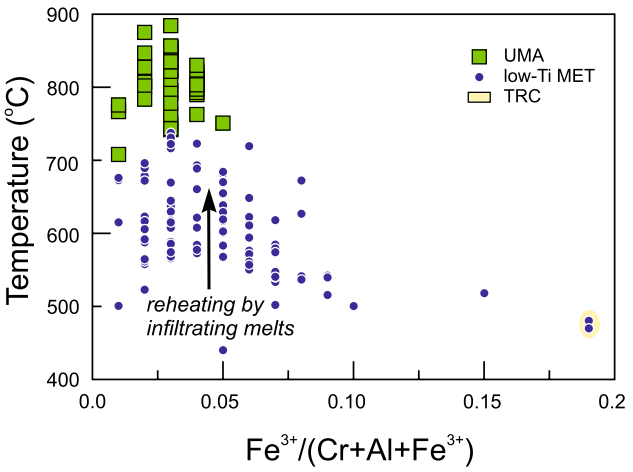

Fig. 11 Temperature vs. Fe^{3+}/ Cr + Al + Fe^{3+} vs. Cr# spinel of metamorphosed Cr–spinel and Ti-rich chromite vs. unmetamorphosed Cr–spinel. *UMA* unmetamorphosed mantle array, *MET* Ti-rich metamorphic, *TRC* Ti-rich chromite

A study of whole-rock chemistry of Expedition 357 peridotite (Whattam et al., 2022) showed that M0071 western serpentinite and M0069 central site peridotite exhibit trace element patterns akin to MOR serpentinite dominated by fluid–rock reactions, whereas the remaining central sites M0072 and M0076 and eastern site serpentinite exhibit patterns similar to MOR peridotite dominated by melt–rock reactions. In this study, we showed that principal variations in the nature of Expedition 357 serpentinite are: (1) the lack of metamorphism recorded in western site serpentinite, which was also not subjected to mafic melt-impregnation and (2) the clear record of greenschist to lower amphibolite facies metamorphism recorded by most serpentinites of the central and eastern sites, many of which are melt impregnated. In contrast to unmetamorphosed mantle array Cr–spinel from western site M0071 serpentinite, which plots within the MOR abyssal peridotite array (Fig. 5), most central and eastern site peridotite Cr–spinel compositions are shifted to the right of the MOR peridotite field indicative of Fe–Mg exchange and Fe^{2+} addition to Cr–spinel and a resulting lowering of Mg#.

When Cr–spinel compositions from fluid–rock dominated central site M0069A and melt–rock dominated central site M0076B (Whattam et al. 2022) are parsed, clear differences in the degree of metamorphism and extent of melt–rock reaction are apparent, with the latter site recording much more evidence of higher degrees of metamorphism (Fig. 12). Although the majority of M0069A serpentinite Cr–spinel compositions follow a horizontal trend and plot

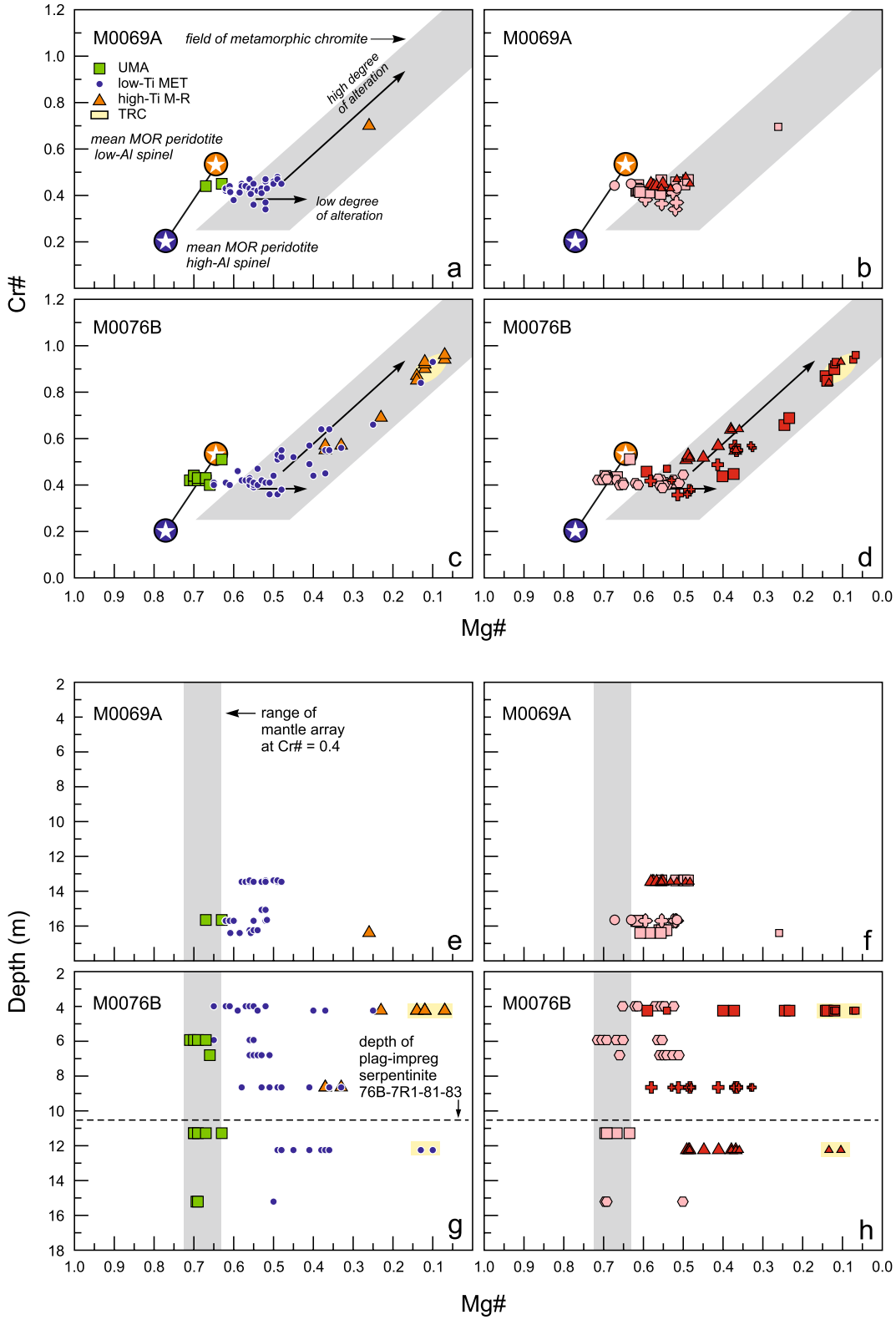

Fig. 12 **a–d** Cr# vs. Mg# and **e–h** depth vs. Mg# of spinel of central sites M0069A and M0076B serpentinites. Symbols in **b**, **d**, **f**, **h** as in Fig. 1d. *UMA* unmetamorphosed mantle array, *MET* metamorphic, *M-R* melt reacted, *TRC* Ti-rich chromite

to the right of the MOR peridotite field consistent with low degrees of metamorphism (greenschist, ~ < 500 °C), apart from one Cr–spinel rim (Roujémon et al., 2018a), there is otherwise no evidence of high degrees of metamorphism. In contrast, serpentinites of central site M0076 record high degrees of Al–Cr exchange and metamorphism ranging up to lower amphibolite facies. Figure 12 also shows that high degrees of metamorphism were achieved within about 5 m above or below plagioclase-impregnated harzburgite M0076B-7R1-81-83 suggesting that the magmatic source of the impregnating melt provided heat to induce contact metamorphism.

Furthermore, there is evidence of metamorphism and melt–rock reactions preserved in individual samples. For example, in central site Type II melt-impregnated harzburgite, 76B-6R1-65-68, a large ~ 1 mm metamorphosed Cr–spinel, is in close proximity to a much smaller 100 µm melt-reacted Cr–spinel (Fig. 3e, f). Two other samples, central Type I serpentinized dunite 76B-3R1-78-82 and eastern site Type II melt-impregnated serpentinite 68B-4R1-23-29 also comprise both metamorphosed and melt-reacted Cr–spinel.

An explanation needs to be provided to explain why the M0069A fluid-dominated serpentinite shows any sign of metamorphism, albeit low grade, in contrast to, for example, the fluid-dominated M0071 western site peridotite, which shows no sign of metamorphism. Evidence of low-grade metamorphism in the M0069A peridotite may be the result of three different possible causes and/or a combination of these causes. (1) Whereas igneous rocks of Expedition 357 are predominantly serpentinite, those of Expedition Sites 304/305 to the NW (Fig. 1a) consist almost entirely of olivine-rich mafic intrusive rocks (Drouin et al. 2009; Ferrando et al. 2018; Godard et al. 2009; Suhr et al. 2008). As shown in Fig. 1a, central Site M0069 is approximately 1 km to the north of western site M0071 and hence closer to mafic intrusive rocks of Expedition 304/305 sites. (2) Hitherto unrecognized, deeper-seated intrusions greater than the length of the core recovered from Site M0069A exist beneath Site M0069A. (3) Site M0069A is in very close proximity (< 0.5 km) to melt-dominated central Sites M0076B and M0072B (see Fig. 1a). In contrast, unmetamorphosed western Site M0071 is ~ 3–4 km to the SW of central sites M00672, M0069B and M0076B. All of these observations can potentially explain a greater influence of heat from nearby magma intrusions on Site M0069 relative to western Site M0071.

Evidence from whole-rock compositions

On the basis of whole-rock chemistry, Whattam et al. (2022) showed that LREE/HREE fractionation, ΣREE, and HFSE (Th, Hf, Zr, Nb, Ti) abundances are highest in Type II melt-impregnated serpentinite in central site M0072 and eastern site M0068. To determine whether the host serpentinite of metamorphosed Cr–spinel records evidence of melt–rock interaction, and hence whether contact metamorphism of diapirs, which impregnated the serpentinite may have caused the metamorphism, in Fig. 13 we plot the mean Mg# of unmetamorphosed, metamorphosed and melt-reacted Cr–spinel and chromite cores and rims ($n = 73$) of a given sample, vs. their corresponding whole-rock abundances of La/Yb, ΣREE, Nb, and Hf (Whattam et al. 2002). The results shown in Fig. 13 unambiguously show a direct relationship between Types II and III central and eastern serpentinite constrained as metamorphic on the basis of Cr–spinel composition and as melt reacted based on whole-rock composition. Cr–spinel with the highest concentrations of La/Yb, ΣREE, Nb, and Hf are metamorphic and from Type II melt-impregnated eastern site serpentinite followed by Type III Si-metasomatized eastern site serpentinite and Type II melt-impregnated serpentinite of the central sites.

Petrogenetic models

Model I: prograde metamorphism

The clear relation between melt reaction and metamorphism and lack of textural evidence to support retrograde metamorphism (see next section) leads us to propose a model of prograde metamorphism. Heat generated by small diapirs associated with magma injection and subsequent melt-impregnation into the central and eastern site peridotite resulted in localized contact metamorphism. Whereas mafic melt-impregnation resulted in production of high TiO_2 Cr–spinel and chromite, greenschist facies metamorphism resulted in Mg–Fe^{2+} exchange between Cr–spinel and forsterite and amphibolite facies metamorphism resulted in Al loss from chromite, possibly due to equilibration with fluids in equilibrium with chlorite. Heat generation may have been facilitated either by circulation of fluids in the impregnated magma, or as the result of recirculation of fluids within the impregnated peridotite. To our knowledge, such a relation between mafic melt-impregnation of peridotite and subsequent prograde metamorphism of peridotite has not previously been corroborated. In Fig. 14, we provide a synopsis of metamorphic and melt–rock reactions undergone by Atlantis Massif serpentinites.

Model II: retrograde metamorphism

An alternative model is that of retrograde metamorphism whereby plagioclase crystallized in the central and eastern site melt-infiltrated rocks only and then broke down to chlorite during serpentinization, which in turn altered the spinel

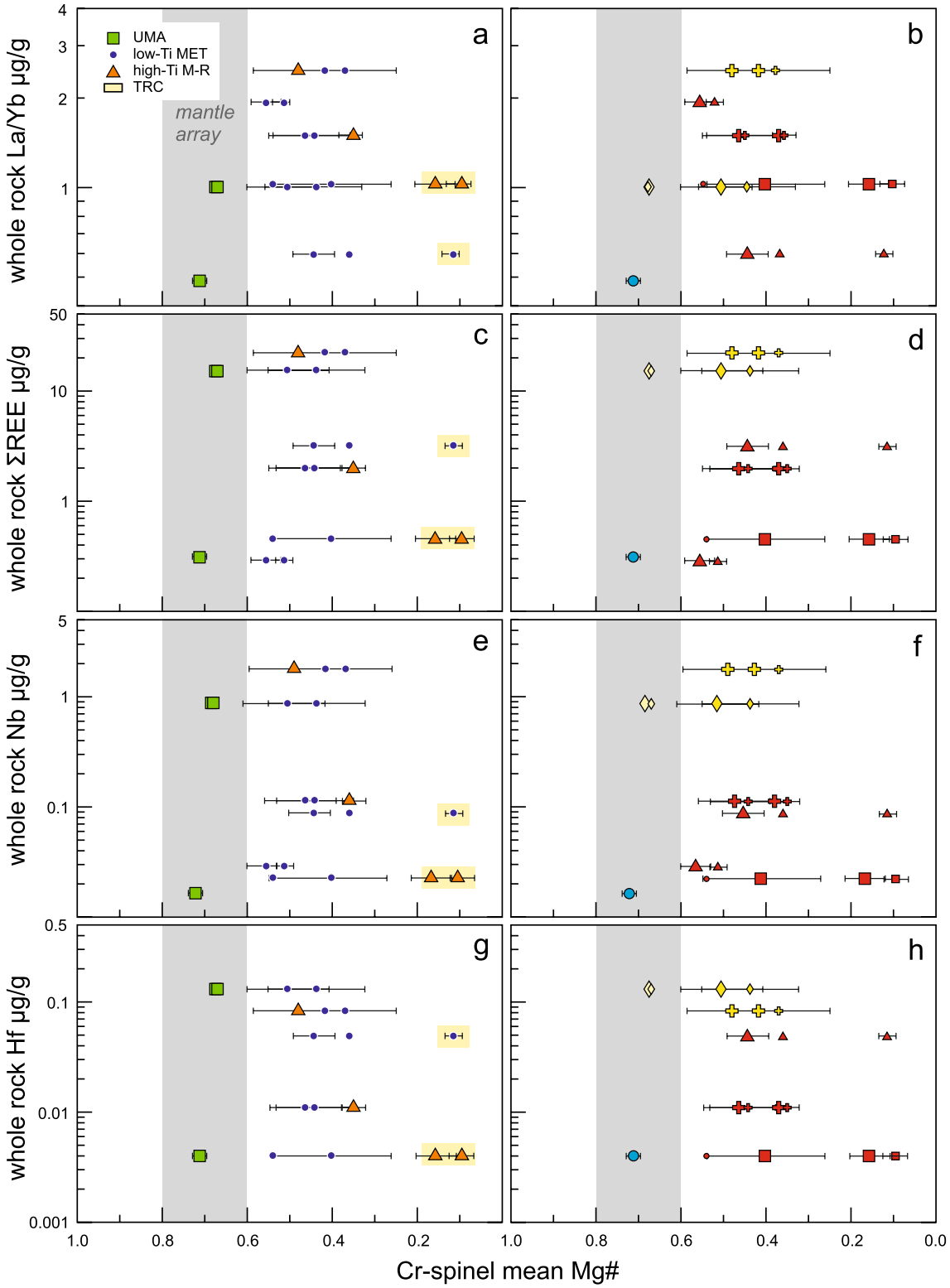

Fig. 13 Mg# of Cr–spinel and chromite vs. whole rock (**a**, **b**) La/Yb, (**c**, **d**) ΣREE, (**e**, **f**) Nb and (**g**, **h**) Hf. Means are of core and rim analyses within a single sample. In the cases where there is no error bar shown, this indicates that there was either only one analysis or that the size of the error bar is less than the size of the symbol. Large errors as exhibited by some samples is related in part to the fact that different spinel, even within the same sample, are highly heterogeneous (spinel within the same sample of course have identical whole-rock compositions). Symbols in **b**, **d**, **f**, **h** are as in Fig. 1d. *UMA* unmetamorphosed mantle array, *MET* metamorphic, *M-R* melt reacted, *TRC* Ti-rich chromite

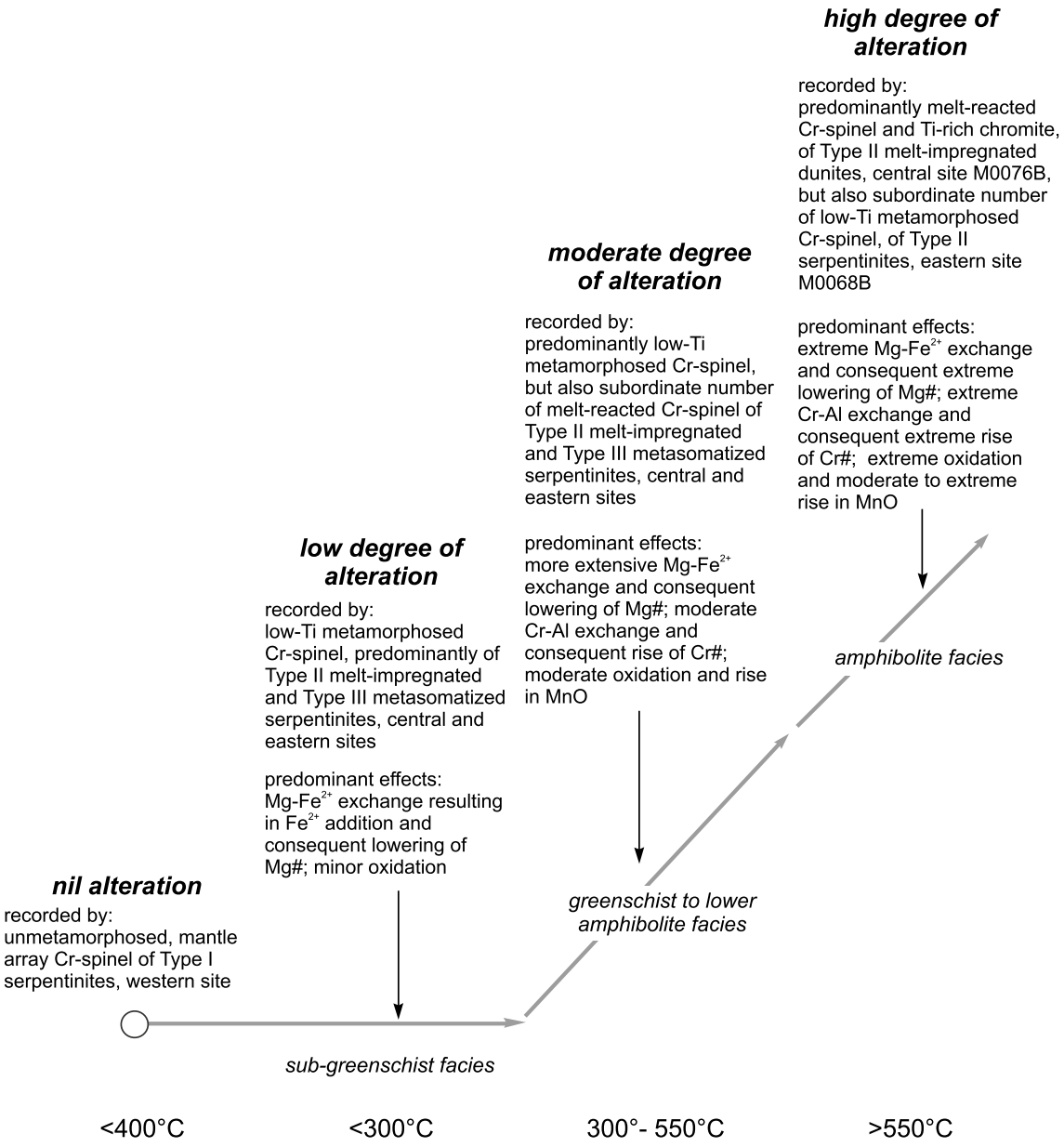

Fig. 14 Synopsis of metamorphic conditions undergone by Expedition 357 serpentinites as recorded by Cr–spinel

composition. In such a scenario, in the western site peridotite that underwent fluid interaction only, no plagioclase, and hence chlorite, formed, and therefore spinel was not affected. Metamorphic formation of hornblende + chlorite may then modify the Cr# and TiO_2 contents of spinel. If this were the case, one would expect hornblende + chlorite coronas occurring at boundaries between olivine and plagioclase, as these phases would be replaced by altered minerals by the progression of serpentinization at lower temperatures, and possibly chlorite in the melt-infiltrated rocks as haloes around spinel (Merlini et al. 2009). However, these features are not observed in the Atlantis Massif peridotite. Critically, in the case of Atlantis Massif peridotite, there is almost nil evidence of plagioclase or hornblende. For example, Whattam et al. (2022) report only one peridotite (of 29) with plagioclase (two tiny grains) and of recent papers which studied Atlantis Massif peridotite (Boshi et al. 2008; Fruh-Green et al. 2018; Roumejon et al. 2018; Akizawa et al. 2020; Whattam et al. 2022), but none report the presence of hornblende in peridotite.

Conclusions

Three kinds of Cr–spinel are distinguished in serpentinized mantle rocks from the Atlantic Massif: (I) primary, unmetamorphosed mantle array, (II) low-Ti metamorphosed, and

(III) high-Ti melt reacted. All Cr–spinel of western site Type I serpentinite are unmetamorphosed ($n = 34$) and comprise 68% of the unmetamorphosed Cr–spinel. Metamorphosed Cr–spinel ($n = 100$) occurs in the central and eastern site serpentinite, whereas melt-reacted Cr–spinel and chromite are restricted to the central sites and occur predominantly in dunite. Estimates of the degree of melt extraction of unmetamorphosed serpentinite using $F = 10\ln(\text{spinel Cr\#}) + 24$ are ~ 9–17%. Fugacity calculations of unmetamorphosed Cr–spinel yield $\Delta\log(fO_2)$FMQ of −1.7 to + 1.0 and a mean closure temperature of 808 ± 39 °C. Mafic melt-impregnation resulted in Cr–spinel with anomalously high TiO_2 of 0.27–0.68 wt.% and production of chromite with up to 1.23 wt.% TiO_2. Greenschist facies metamorphism (< 500°) resulted in Mg–Fe^{2+} exchange between Cr–spinel and forsterite and anomalously low Cr–spinel Mg#; higher degrees of lower amphibolite facies metamorphism (> 600 °C) also resulted in anomalously high Cr# due to Al–Cr exchange. A clear relationship exists between melt-impregnation and metamorphism of central and eastern serpentinites, as shown in Cr–spinel vs. whole-rock compositions, which we postulate to be the result of heat associated with magma injection and subsequent localized, contact metamorphism. Closure temperatures of 440–731 °C of metamorphosed Cr–spinel approximate greenschist to amphibolite facies metamorphic conditions.

Supplementary Information The online version contains supplementary material available at https://doi.org/10.1007/s00410-022-01968-9.

Acknowledgements This research used samples and data provided by the International Ocean Discovery Program (IODP). This project would not have been possible without the support of the entire IODP Expedition 357 scientific party and support staff from the ECORD Science Operator. We thank Co-chief Scientists Gretchen Früh-Green and Beth Orcutt, Expedition Project Managers Carol Cotterill and Sophie Green, Offshore Operations Manager David Smith, the ESO Laboratory and Curation Manager Ursula Röhl, and the entire team of the Bremen Core Repository at MARUM. Funding for Expedition 357 was provided by the European Consortium for Ocean Research Drilling (ECORD). SAW acknowledges financial support from the Korea International Ocean Discovery Program (K-IODP) funded by the Ministry of Oceans and Fisheries, Korea and KFUPM for funds from Project# SF18068 and SF18069 awarded to SAW. MIL acknowledges that this research was undertaken thanks in part to funding from the Canada First Research Excellence Fund through the Arthur B. McDonald Canadian Astroparticle Physics Research Institute. We thank Editor Tim Grove, Shoji Arai and an anonymous reviewer for constructive comments which improved the manuscript.

References

Absalov MZ (1998) Chrome-spinels in gabbro-wehrlite intrusions of the Pechenga area, Kola Peninsula, Russia: emphasis on alteration features. Lithos 43:109–134

Akizawa N, Früh-Green GL, Tamura C, Morishita T (2020) Compositional heterogeneity and melt transport in mantle beneath Mid-Atlantic Ridge constrained by peridotite, dunite, and wehrlite from Atlantis Massif. Lithos 354–355:105364. https://doi.org/10.1016/j.lithos.2019.105364

Andreani M, Mevel C, Boullier, A-M, Escartin J, (2007) Dynamic control on serpentine crystallization in veins: constraints on hydration processes in oceanic peridotites. Geochemistry, Geophysics, Geosystems 8.

Ara S, Shimizu Y, Ismail SA, Ahmed AH (2006) Low-T formation of high-Cr spinel with apparently primary chemical characteristics within podiform chromitite from Rayat, northeastern Iraq. Mineral Mag 70(5):499–508

Arai S, Yurimoto H (1994) Podiform chromitites of the Tari-Misaka ultramafic complex, southwestern Japan, as mantle-melt interaction products. Econ Geol 89:1279–2188

Arai S, Abe N, Hirai H (1998) Petrological characteristics of the subarc mantle: an overview on petrology of peridotite xenoliths from the Japan Arcs. Trends in Mineralogy 2:39–55

Arai S, Matsukage K (1996) Petrology of gabbro-troctolite–peridotite complex from Hess Deep, equatorial Pacific: implications for mantle–melt interaction within the oceanic lithosphere. In: Mével C, Gillis KM, Allan JF, Meyer PS (Eds.), Proceedings of the Ocean Drilling Program: Scientific Results, 147:135–155.

Aswad KJA, Aziz NRH, Koyi HA (2011) Cr–spinel compositions in serpentinites and their implications for the petrotectonic history of the Zagros Suture Zone, Kurdistan Region. Iraq Geological Magazine 148(5–6):802–818. https://doi.org/10.1017/S0016756811000422

Ballhaus C, Berry RF, Green DH (1990) Oxygen fugacity controls in the Earth's upper mantle. Nature 348:437–440. https://doi.org/10.1038/348437a0

Ballhaus C, Berry RF, Green DH (1991) High pressure experimental calibration of the olivine-orthopyroxene-spinel oxygen barometer, implications for the oxidation of the mantle. Contrib Miner Petrol 107:27–40

Barnes SJ (2000) Chromite in komatiites II. Modification during greenschist to mid-amphibolite facies metamorphism. J Petrol 41:387–409

Barnes SJ, Roeder PL (2001) The range of spinel compositions in terrestrial mafic and ultramafic rocks. J Petrol 42(12):2279–2302

Barra F, Gervilla F, Hernández E, Reich M, Padrón-Navarta JA, González-Jiménez JM (2014) Alteration patterns of chromian spinels from La Cabaña peridotite, south-central Chile. Mineral Petrol 108:819–836. https://doi.org/10.1007/s00710-014-0335-5

Bedini RM, Bodinier J-L (1999) Distribution of incompatible trace elements between the constituents of spinel peridotite xenoliths: ICP-MS data from the East African Rift. Geochim Cosmochim Acta 63(22):3883–3900

Berger ET, Vannier M (1984) Les dunites en enclaves dans les basaltes des îles océaniques alcalins: Approache pétrologique. Bulletin Minéralogie 107:649–663

Bhat IM, Ahmad T, Subba Rao DV (2019) Alteration of primary Cr–spinel mineral composition from the Suru Valley ophiolitic peridotites, Ladakh Himalaya: Their low-temperature metamorphic implications. J Earth Syst Sci 128:188. https://doi.org/10.1007/s12040-019-1222-6

Blackman DK, Cann JR, Janssen B, Smith DK (1998) Origin of extensional core complexes: evidence from the Mid-Atlantic Ridge at Atlantis Fracture Zone. Journal of Geophysical Research: Solid Earth 103:21315–21333

Blackman DK, Karson JA, Kelley DS, Cann JR, Früh- Green GL, Gee JS, Hurst SD, John BE, Morgan J, Nooner SL, Ross DK, Schroeder TJ, Williams EA (2002) Geology of the Atlantis Massif (Mid-Atlantic Ridge, 30°N): Implications for the evolution of an ultramafic oceanic core complex. Mar Geophys Res 23:443–469

Blackman DK, Ildefonse B, John BE, Ohara Y, Miller DJ, MacLeod CJ (2006) Proceedings of the IODP, 304/305. College Station TX. https://doi.org/10.2204/iodp.proc.304305.2006

Blanco-Quintero IF, Proenza JA, García-Casco A, Tauler E, Galí S (2011) Serpentinites and serpentinites within a fossil subduction channel: La Corea mélange, eastern Cuba. Geol Acta 9(3–4):389–405. https://doi.org/10.1344/105.000001662

Bodinier JL, Menzies MA, Thirlwall MF (1991) Continental to oceanic mantle transition: REE and Sr–Nd isotopic geochemistry of the Lanzo Lherzolite Massif. Journal of Petrology Special 2:191–210

Bodinier JL, Godard M (2003) Orogenic, ophiolitic, and abyssal peridotites. Treatise on Geochemistry, vol. 2. Elsevier, Amsterdam, pp. 103–170.

Borghini G, Rampone E (2007) Postcumulus processes in oceanic-type olivine-rich cumulates: the role of trapped melt crystallization versus melt/rock interaction. Contrib Mineral Petrol 154(6):619–633

Borghini G, Rampone E, Crispini L, De Ferrari R, Godard M (2007) Origin and emplacement of ultramafic–mafic intrusions in the Erro-Tobbio mantle peridotite (Ligurian Alps, Italy). Lithos 94(1):210–229

Boschi C, Früh-Green GL, Delacour A, Karson JA, Kelley DS (2006a) Mass transfer and fluid flow during detachment faulting and development of an oceanic core complex, Atlantis Massif (MAR 30°N). Geochem Geophys Geosyst 7(1):Q01004

Boschi C, Früh-Green GL, Escartin J (2006b) Occurrence and significance of serpentinite-hosted, talc-rich fault rocks in modern oceanic settings and ophiolite complexes. Ofioliti 31(2):123–134

Burkhard DJM (1993) Accessory chromian spinels: Their coexistence and alteration in serpentinites. Geochim Cosmochim Acta 57:1297–1306

Cann JR, Blackman DK, Smith DK, McAllister E, Janssen B, Mello S, Avgerinos E, Pascoe AR, Escartín J (1997) Corrugated slip surfaces formed at ridge-transform intersections on the Mid-Atlantic Ridge. Nature 385:329–332

Cannat M (1993) Emplacement of mantle rocks in the seafloor at mid-ocean ridges. J Geophys Res 98(B3):4163–4172

Cannat M, Bideau D, Hebert R (1990) Plastic deformation and magmatic impregnation in serpentinized ultramafic rocks from the Garrett transform fault (East Pacific Rise). Earth Planet Sci Lett 101(2):216–232

Cannat M, Karson JA, Miller DJ, Agar, SM, Barling J, Casey JF, Ceuleneer G, Dilek Y, Fletcher JM, Fujibayashi N, Gaggero L, Gee JS, Hurst SD, Kelley DS, Kempton PD, Lawrence RM, Marchig V, Mutter C, Niida K, Rodway K, Ross DK, Stephens CJ, Werner C-D, Whitechurch H (1995) Mid-Atlantic Ridge: Sites 920–924. Proc. ODP, Initial Reports, 153. Ocean Drilling Program, Texas A&M University, College Station, TX, United States.

Dare SAS, Pearce JA, McDonald I, Styles MT (2009) Tectonic discrimination of peridotites using fO_2–Cr# and Ga–Ti–Fe^{III} systematics. Chem Geol 261:199–216

Dick HJB, Bullen T (1984) Chromian spinel as a petrogenetic indicator in abyssal and alpine-type peridotites and spatially associated lavas. Contrib Miner Petrol 86:54–76

Dick HJB, Natland JH (1996) Late-stage melt evolution and transport in the shallow mantle beneath the east Pacific rise. Proc Ocean Drill Program Sci Results 147:103–134

Dick HJB, Natland JH, Alt JC, Bach W, Bideau D, Gee JS, Haggas S, Hertogen JGH, Hirth G, Holm PM, Ildefonse B, Iturrino G, John BE, Kelley DS, Kikawa E, Kingdon A, LeRoux PJ, Maeda J, Meyer PS, Miller DJ, Naslund HR, Niu Y, Robinson PT, Snow JE, Stephen RA, Trimby PW, Worm H-U, Yoshinobu A (2000) A long in situ section of the lower ocean crust: results of ODP Leg 176 drilling at the Southwest Indian Ridge. Earth Planet Sci Lett 179:31–51

Donnelly KE, Goldstein SL, Langmuir CH, Spiegelman M (2004) Origin of enriched ocean ridge basalts and implications for mantle dynamics. Earth Planet Sci Lett 226:347–366

Drouin M, Godard M, Ildefonse B, Bruguier O, Garrido CJ (2009) Geochemical and petrographic evidence for magmatic impregnation in the oceanic lithosphere at Atlantis Massif, Mid-Atlantic Ridge (IODP Hole U1309D, 30°N). Chem Geol 264:71–88

Evans BW, Frost BR (1975) Chrome-spinel in progressive metamorphism; a preliminary analysis. Geochim Cosmochim Acta 39:959–972

Evans BW, Trommsdorff V (1970) Regional metamorphism of ultramafic rocks in the Central Alps Paragenesis in the system CaO–MgO–SiO_2–H_2O. Schweiz Min Pen Milt 50:481–492

Ferrando C, Godard M, Ildefonse B, Rampone E (2018) Melt transport and mantle assimilation at Atlantis Massif (IODP Site U1309): constraints from geochemical modeling. Lithos 323:24–43

Frisby C, Bizimis M, Mallick S (2016) Seawater-derived rare earth element addition to abyssal peridotites during serpentinization. Lithos 248–251:432–454

Früh-Green GL, Orcutt BN, Rouméjon S et al (2018) Magmatism, serpentinization and life: insights through drilling the Atlantis Massif (IODP Expedition 357). Lithos 323:137–155. https://doi.org/10.1016/j.lithos.2018.09.012

Früh-Green GL, Connolly JAD, Plas A, Kelley DS, Grobéty B (2004) Serpentinization of oceanic peridotites: implications for geochemical cycles and biological activity. In: Wilcock, W.S.D., DeLong, E.F., Kelley, D.S., Baross, J.A., Cary, C. (Eds.), The Subseafloor Biosphere at Mid-Ocean Ridges. Geophysical Monograph. 144, pp. 119–136.

Früh-Green GL, Orcutt BN, Green S, Cotterill C and the Expedition 357 Scientists, 2016. Expedition 357 Preliminary Report: Atlantis Massif Serpentinization and Life. International Ocean Discovery Program. https://doi.org/10.14379/iodp.pr.357.2016

Früh-Green GL, Orcutt BN, Green SL et al. (2017) Expedition 357 summary. In: Früh- Green, G.L., Orcutt, B.N., Green, S.L., Cotterill, C. (Eds.), Expedition 357 Scientists. Proceedings of the International Ocean Discovery Program 357, College Station, TX. https://doi.org/10.14379/iodp.proc.357.101.2017.

Gargiulo MF, Bjerg EA, Mogessie A (2013) Spinel group minerals in metamorphosed ultramafic rocks from Río de Las Tunas belt, Central Andes. Argentina Geologica Acta 11(2):133–148. https://doi.org/10.1344/105.000001836

Godard M, Lagabrielle Y, Alard O, Harvey J (2008) Geochemistry of the highly depleted peridotites drilled at ODP Sites 1272 and 1274 (Fifteen–Twenty Fracture Zone, Mid-Atlantic Ridge): implications for mantle dynamics beneath a slow spreading ridge. Earth Planet Sci Lett 267(3–4):410–425. https://doi.org/10.1016/j.epsl.2007.11.058

Godard M, Awaji S, Hansen H et al (2009) Geochemistry of a long in-situ section of intrusive slow-spread oceanic lithosphere: results fromIODP Site U1309 (Atlantis Massif, 30°N Mid-Atlantic-Ridge). Earth Planet Sci Lett 279:110–122

González-Jiminéz JM, Kerestedjian T, Proenza JA, Gervilla F (2009) Metamorphism on Chromite Ores from the Dobromirtsi Ultramafic Massif, Rhodope Mountains (SE Bulgaria). Geologica Acta 67 7(4):413–429. https://doi.org/10.1344/104.000001447.

Grimes CB, John BE, Cheadle MJ, Wooden JL (2008) Protracted construction of gabbroic crust at a slow spreading ridge: constraints from 206Pb/238U zircon ages from Atlantis Massif and IODP Hole U1309D (30°N, MAR). Geochem Geophys Geosyst 9:Q08012

Grove TL, Kinzler RJ, Brian WB (1992) Fractionation of mid-ocean ridge basalt. In: Morgan, J.P., Blackman, D.K., Sinton, J.M. (Eds.), Mantle Flow and Generation at Mid-ocean Ridges, vol. 71. Geophysical Monograph, American Geophysical Union, pp. 281e311.

Hart SR, Zindler A (1986) In search of a bulk-earth composition. Chem Geol 57:247–267

Heinrich KFJ (1987) Mass absorption coefficients for electron probe microanalysis. In: Brown, J. Packwood, R. (Eds.), Proceedings of the 11th International Congress on X-Ray Optics and Microanalysis, University of Western Ontario, London, Ontario, Canada 1986, pp. 67–119.

Hellebrand E, Snow JE, Dick HJB, Hofmann AW (2001) Coupled major and trace elements as indicators of the extent of melting in mid-ocean-ridge peridotites. Nature 410:677–681

De Hoog JCM, Janák M, Vrabec M, Hattori KH (2011) Ultramafic cumulates of oceanic affinity in an intracontinental subduction zone: ultrahigh-pressure garnet peridotites from Pohorje (Eastern Alps, Slovenia). In: "Ultrahigh-Pressure Metamorphism: 25 years after the discovery of coesite and diamond" Eds: L. Dobrzhinetskaya et al. Elsevier, Amsterdam:399–439.

Ildefonse B, Blackman DK, John BE, Ohara Y, Miller DJ, MacLeod CJ (2007) Oceanic core complexes and crustal accretion at slow-spreading ridges. Geology 35:623–626

Irvine TN (1967) Chromian spinel as a petrogenetic indicator Part 2, petrologic applications. Can J Earth Sci 4:71–103

Jagoutz E, Palme H, Baddenhausen H, Blum K, Cendales M, Dreibus G, Spettel B, Lorenz V, Vanke H (1979) The abundance of major, minor and trace elements in the earth's mantle as derived from primitive ultramafic nodules. Geochim Cosmochim Acta 11(2):2031–2050

Karson JA (2002) Geologic structure of the uppermost oceanic crust created at fast- to intermediate-rate spreading centers. Annu Rev Earth Planet Sci 30:347–384

Karson JA, Früh-Green GL, Kelley DS, Williams EA, Yoerger DR, Jakuba M (2006) Detachment shear zone of the Atlantis Massif core complex, Mid-Atlantic Ridge, 30°N. Geochem Geophys Geosyst 7(6):Q06016

Kelemen PB (1990) Reaction between ultramafic rock and fractionating basaltic magma I. Phase relations, the origin of calc-alkaline magma series, and the formation of discordant dunite. J Petrol 31:51–98

Kelemen PB, Joyce DB, Webster JD, Holloway JR (1990) Reaction between ultramafic rock and fractionating basaltic magma. 2. Experimental investigation of reaction between olivine tholeiite and harzburgite at 1150 °C–1050 °C and 5 kb. J Petrol 31:99–134

Kelemen PB, Dick HJ, Quick JE (1992) Formation of dunite by pervasive melt/rock reaction in the upper mantle. Nature 358:635–641

Kelemen PB, Hitehead JA, Aharonov E, Jordahl KA (1995a) Experiments on flow focusing in soluble porous media, with applications to melt extraction from the mantle. J Geophys Res 100:475–496

Kelemen PB, Shimizu N, Salters VJM (1995b) Extraction of mid-ocean-ridge basalt from the upwelling mantle by focused flow of melt in dunite channels. Nature 375:747–753

Kelemen PB, Hirth G, Shimizu N, Spiegelman M, Dick H (1997) A review of melt migration processes in the adiabatically upwelling mantle beneath oceanic spreading ridges. Philosophical Trans R Soc Lond Ser A355:283–318

Kelemen P, Kikawa E, Miller J, Abe N, Bach W, Carlson RL, Casey JF, Chambers, LM, Cheadle M, Cipriani A, Dick HJB, Faul U, Garces M, Garrido C, Gee JS, Godard M, Griffin DW, Harvey J, Ildefonse B, Iturrino GJ, Josef J, Meurer WP, Paulick H, Rosner M, Schroeder T, Seyler M, Takazawa E, Mrozewski S (2004) Drilling Mantle Peridotite along the Mid-Atlantic Ridge from 14° to 16°N: Sites 1268–1275. Proc. ODP, Initial Reports, 209. Ocean Drilling Program, Texas A&M University, College Station TX 77845–9547, USA. https://doi.org/10.2973/odp.proc.ir.209.2004 pp.

Kelemen PB, Kikawa E, Miller DJ, Shipboard Scientific Party (2007) Leg 209 summary: processes in a 20-km-thick conductive boundary layer beneath the Mid-Atlantic Ridge, 14°–16°N. In: Kelemen, P.B., Kikawa, E., Miller, D.J. (Eds.), Proceedings of the Ocean Drilling Program, Scientific Results, 209: College Station, TX. Ocean Drilling Program, pp. 1–33.

Kelley DS, Karson JA, Blackman DK, Früh-Green GL, Butterfield DA, Lilley MD, Olson EJ, Shrenk MO, Roe KK, Lebon GT, Rivizzigno P (2001) An off-axis hydrothermal vent field discovered near the Mid-Atlantic Ridge at 30°N. Nature 412:145–149

Khalil KI, El-Makky AM (2009) Alteration mechanisms of chromian-spinel during serpentinization at Wadi Sifein Area, Eastern Desert. Egypt Resource Geology 59(2):194–211. https://doi.org/10.1111/j.1751-3928.2009.00090.x

Khedr MZ, Arai S (2013) Origin of Neoproterozoic ophiolitic peridotites in south Eastern Desert, Egypt, constrained from primary mantle mineral chemistry. J Mineral Petrol 107(5):807–828

Khedr MZ, Takazawa E, Hauzenberger C, Tamura A, Arai S, Stern RJ, Morishita T, El-Awady A (2022) Petrogenesis of arc-related serpentinized peridotites (Egypt): Insights into Neoproterozoic mantle evolution beneath the Arabian-Nubian Shield. J Asian Earth Sci 226:105078

Kimball KL (1990) Effects of hydrothermal alteration on the compositions of chromian spinels. Contrib Miner Petrol 105:337–346

Lambart S, Laporte D, Schiano P (2013) Markers of the pyroxenite contribution in the major element compositions of oceanic basalts: Review of the experimental constraints. Lithos 160–161:14–36. https://doi.org/10.1016/j.lithos.2012.11.018

Le Roux PJ, Le Roex AP, Schilling J-G, Shimizu N, Perkins WW, Pearce NJG (2002) Mantle heterogeneity beneath the southern Mid-Atlantic Ridge: trace element evidence for contamination of ambient asthenospheric mantle. Earth Planet Sci Lett 203(1):479–498

Lenoir X, Garrido CJ, Bodinier J-L, Dautria J-M, Gervilla F (2001) The recrystallization front of the Ronda peridotite: evidence for melting and thermal erosion of subcontinental lithospheric mantle beneath the Alboran Basin. J Petrol 42:141–158

Lyubetskaya T, Korenaga J (2007) Chemical composition of Earth's primitive mantle and its variance: 1. Method Results J Geophys Res 12:B03211. https://doi.org/10.1029/2005JB004223

Macdonald KC (1982) Mid-ocean ridges: Fine scale tectonic, volcanic and hydrothermal processes within the plate boundary zone. Annu Rev Earth Planet Sci 10:155–190

Manatschal G, Müntener O (2009) A type sequence across an ancient magma-poor ocean-continent transition: the example of the western Alpine Tethys ophiolites. Tectonophysics 473:4–19

McDonough WF, Rudnick RL (1998) Mineralogy and composition of the upper mantle. In: Hemley, R.J. (Ed.), Ultrahigh pressure mineralogy: Reviews in Mineralogy, V. 37, Mineralogical Society

of America, DeGruyter, pp. 139–164. https://doi.org/10.1515/9781501509179.
McDonough WF, Sun SS (1995) The composition of the Earth. Chem Geol 120:223–253
Merlini A, Grieco G, Diella V (2009) Ferritchromite and chromian-chlorite formation in mélange-hosted Kalkan chromitite (Southern Urals, Russia). Am Miner 94:1459–1467
Müntener O, Pettke T, Desmurs L, Meier M, Schaltegger U (2004) Refertilization of mantle peridotite in embryonic ocean basins: trace element and Nd isotopic evidence and implications for crust–mantle relationships. Earth Planet Sci Lett 221:293–308. https://doi.org/10.1016/S0012-821X(04)00073-1
Nicolas A, Jackson M (1982) High temperature dikes in peridotites: Origin by hydraulic fracturing. J Petrol 23:568–582
Niida K (1997) Mineralogy of MARK peridotites: replacement through magma channeling examined from 920D, MARK area. In: Karson JA, Cannat M, Miller DJ, Elthon D (Eds.), Proceedings of the Ocean Drilling Program: Scientific Results153. Ocean Drilling Program, College Station, TX, pp. 265–275.
Niu Y (1997) Mantle melting and melt extraction processes beneath ocean ridges: evidence from abyssal peridotites. J Petrol 38:1047–1074
Niu Y (2004) Bulk rock major and trace element compositions of abyssal peridotites: implications for mantle melting, melt extraction and post-melting processes beneath mid-ocean ridges. J Petrol 45:2423–2458
O'Hanley DS (1996) Serpentinites records of tectonic and petrological history. Oxford University Press, Oxford, p 290
Obata M, Banno S, Mori T (1974) The iron-magnesium partitioning between naturally occurring coexisting olivine and Ca-rich clinopyroxene: An application of the simple mixture model to olivine solid solution. Bull Soc Jr Miner Crystallogr 97:101–107
Palme H, O'Neill HSC (2003) Cosmochemical estimates of mantle composition. In: Holland H, Turekian KK (eds) Treatise on Geochemistry, vol 2. Elsevier, New York, pp 1–38
Parkinson IJ, Pearce JA (1998) Peridotites from the Izu–Bonin–Mariana Forearc (ODP Leg 125), evidence for mantle melting and melt–mantle interaction in a suprasubduction zone setting. J Petrol 39:1577–1618
Paulick H, Bach W, Godard M, De Hoog JCM, Suhr G, Harvey J (2006) Geochemistry of abyssal peridotites (Mid-Atlantic Ridge, 15°20′N, ODP Leg 209): implications for fluid/rock interaction in slow spreading environments. Chem Geol 234:179–210
Picazo S, Muntener O, Manatschal G, Bauville A, Karner G, Johnson C (2016) Mapping the nature of mantle domains in Western and Central Europe based on clinopyroxene and spinel chemistry: evidence for mantle modification during an extensional cycle. Lithos 266–267:233–263. https://doi.org/10.1016/j.lithos.2016.08.029
Pouchou J-L, Pichoir F (1991) Quantitative analysis of homogeneous or stratified microvolumes applying the model "PAP". In: Heinrich, K.F.J., Newbury, D.E. (Eds.), Electron Probe Quantitation Plenum Publishing Corporation, New York, New York, pp. 31–75.
Purvis AC, Nesbitt RW, Hallberg JA (1972) The geology of the part of the Carr Boyd rocks complex and its associated nickel mineralization, Western Australia. Econ Geol 67:1093–1113
Quick JE (1981) The origin and significance of large, tabular dunite bodies in the Trinity peridotite, northern California. Contrib Miner Petrol 78:413–422
Rampone E, Piccardo GB (2000) The ophiolite-oceanic lithosphere analogue: new insights from the Northern Apennine (Italy). In: Dilek J, Moores E, Elthon D, Nicolas A (eds) Ophiolites and Oceanic Crust: New Insights from Field Studies and Ocean Drilling Program, vol 349. Geological Society of America, Special Paper, pp 21–34
Rampone E, Piccardo GB, Vannucci R, Bottazzi P, Zanetti A (1994) Melt-impregnation in ophiolitic peridotite: an ion microprobe study of clinopyroxene and plagioclase. Mineral Mag 58A:756–757
Rampone E, Piccardo GB, Vannucci R, Bottazzi P (1997) Chemistry and origin of trapped melts in ophiolitic peridotites. Geochim Cosmochim Acta 61:4557–4569
Reed SJB (1990) Fluorescence effects in quantitative microprobe analysis. In: Williams, D.B., Ingram, P., Michael, J.R. (Eds.), Microbeam Analysis-1990 San Francisco Press, San Francisco, pp. 109–114.
Renna MR, Tribuzio R (2011) Olivine-rich troctolites from Ligurian ophiolites (Italy): Evidence for impregnation of replacive mantle conduits by MORB-type melts. J Petrol 52(9):1763–1790
Rouméjon S, Cannat M, Agrinier P, Godard M, Andreani M (2015) Serpentinization and Fluid Pathways in Tectonically Exhumed Peridotites from the Southwest Indian Ridge (62–65 E). J Petrol 56:703–734
Rouméjon S, Williams MJ, Früh-Green GL (2018b) In situ oxygen isotope analyses in serpentine minerals: constraints on serpentinization during tectonic exhumation at slow- and ultra-slow-spreading ridges. Lithos 323:156–173. https://doi.org/10.1016/j.lithos.2018.09.021
Rouméjon S, Früh-Green GL, Orcutt BN, IODP Expedition 357 Science Party (2018a) Alteration heterogeneities in peridotites exhumed on the southern wall of the Atlantis Massif (IODP Expedition 357). Journal of Petrology 1–29. https://doi.org/10.1093/petrology/egy065
Sack RO, Ghiorso MS (1991) Chromian spinels as petrogenetic indicators: thermodynamic and petrological applications. Am Miner 76:827–847
Sanfilippo A, Tribuzio R (2013) Origin of olivine-rich troctolites from the oceanic lithosphere: a comparison between the alpine Jurassic ophiolites and modern slow spreading ridges. Ofioliti 38(1):89–99
Sanfilippo A, Dick HJ, Ohara Y (2013) Melt–rock reaction in the mantle: Mantle troctolites from the Parece Vela ancient back-arc spreading center. J Petrol 54(5):861–885
Sanfilippo A, Tribuzio R, Tiepolo M (2014) Mantle–crust interactions in the oceanic lithosphere: Constraints from minor and trace elements in olivine. Geochim Cosmochim Acta 141:423–439
Säntii J, Kontinen A, Sorjonen-Ward P, Johanson B, Pakkanen L (2006) Metamorphism and chromite in serpentinized and carbonate-silica-altered peridotites of the paleoproterozoic Outokumpu-Jormua Ophiolite Belt, eastern Finland. Int Geol Rev 48:494–546. https://doi.org/10.2747/0020-6814.48.6.494
Saumur BM, Hattori K (2013) Zoned Cr–spinel and ferritchromite alteration in forearc mantle serpentinites of the Rio San Juan Complex. Dominican Republic Mineral Mag 77(1):117–136. https://doi.org/10.1180/minmag.2013.077.1.11
Schroeder T, John BE (2004) Strain localization on an oceanic detachment fault system, Atlantis Massif, 30°N, Mid-Atlantic Ridge. Geochemistry, Geophysics, Geosystems 5.
Shibata T, Thompson G (1986) Peridotites from the mid-Atlantic ridge at 43 °N and their petrogenetic relation to abyssal tholeiites. Contribution to Mineralogy and Petrology 93:144–159
Snow JE, Dick HJB (1995) Pervasive magnesium loss by marine weathering of peridotite. Geochim Cosmochim Acta 59(20):4219–4235
Spangenberg K (1943) Die Chromitlagerstatte von Tampadel am Zobten. Zeitschrift Fur Praktische Geologie 51:13–35
Springer G (1971) Fluorescence by the X-ray continuum in multi-element targets: Falconbridge Nickel Mines Limited, Thornhill, Ontario, Canada, Report FRL-138, 14 p.

Stevens RE (1944) Composition of some chromites of the Western hemisphere. Am Miner 29:1–34

Stewart MA, Karson JA, Klein EM (2005) Four-dimensional upper crustal construction at fast-spreading mid-ocean ridges: a perspective from an upper crustal cross-section at the Hess Deep Rift. J Volcanol Geoth Res 144:287–309

Su Y (2003) Global MORB chemistry compilation at the segment scale. Ph.D. Thesis. New York, Columbia University.

Suhr G, Hellebrand E, Snow JE, Seck HA, Hofmann AW (2003) Significance of large, refractory dunite bodies in the upper mantle of the Bay of Islands Ophiolite. Geochem Geophys Geosyst 4:8605. https://doi.org/10.1029/2001GC000277

Suhr G, Hellebrand E, Johnson K, Brunelli D (2008) Stacked gabbro units and intervening mantle: a detailed look at a section of IODP Leg 305, Hole U1309D. Geochem Geophys Geosyst 9:Q10007. https://doi.org/10.1029/2008GC002012

Suita MT, Strieder JA (1996) Cr–spinels from Brazilian mafic-ultramafic complexes: metamorphic modifications. Int Geol Rev 38(245):267

Takahashi N (1992) Evidence for melt segregation towards fractures in the Horoman mantle peridotite complex. Nature 359:52–55

Takazawa E, Frey FA, Shimuzu N, Obata M, Bodinier JL (1992) Geochemical evidence for melt migration and reaction in the upper mantle. Nature 359:55–58

Tucholke BE, Lin J, Kleinrock MC (1998) Megamullions and mullion structure defining oceanic metamorphic core complexes on the Mid-Atlantic Ridge. J Geophys Res 103:9857–9866

Van der Wal D, Bodinier J-L (1996) Origin of the recrystallisation front in the Ronda peridotite by km-scale pervasive porous melt flow. Contrib Miner Petrol 122:387–405

Whattam SA, Cho M, Smith IEM (2011) Magmatic peridotites and pyroxenites, Andong Ultramafic Complex, Korea: Geochemical evidence for supra-subduction zone formation and extensive melt–rock interaction. Lithos 127:599–618

Whattam SA, Früh-Green GL, Cannat, M, De Hoog C-J, Schwarzenbach EM, Escartin J, John BE, Leybourne MI, Williams MJ, Rouméjon S, Akizawa N, Boschi C, Harris M, Wenzel K, McCaig A, Weiss D, Bilenker L (2022) Geochemistry of serpentinized and multiphase altered Atlantis Massif peridotites (IODP Expedition 357): Petrogenesis and discrimination of melt–rock vs. fluid–rock processes. Chemical Geology 594. https://doi.org/10.1016/j.chemgeo.2021.120681.

Workman RK, Hart SR (2005) Major and trace element composition of the depleted MORB mantle (DMM). Earth Planet Sci Lett 231:53–72

Authors and Affiliations

Scott A. Whattam[1] · Jan C. M. De Hoog[2] · Matthew I. Leybourne[3] · Mohamed Zaki Khedr[4]

[1] Department of Geosciences, King Fahd University of Petroleum and Minerals, Dhahran 31261, Saudi Arabia

[2] School of Geosciences, Grant Institute, The University of Edinburgh, James Hutton Road, Edinburgh EH9 3FE, UK

[3] Queen's Facility for Isotope Research, Department of Geological Sciences and Geological Engineering, and Arthur B. McDonald Canadian Astroparticle Physics Research Institute, Department of Physics, Engineering Physics & Astronomy, Queen's University, Kingston, ON K7L 3N6, Canada

[4] Department of Geology, Faculty of Science, Kafrelsheikh University, Kafrelsheikh 33516, Egypt